1996ApJ...465..717L

THE ASTROPHYSICAL JOURNAL, 465:717–732, 1996 July 10

HUBBLE SPACE TELESCOPE ULTRAVIOLET IMAGING AND SPECTROSCOPY OF THE BRIGHT STARBURST IN THE WOLF-RAYET GALAXY NGC 4214[1]

CLAUS LEITHERER,[2] WILLIAM D. VACCA,[3] PETER S. CONTI,[4] ALEXEI V. FILIPPENKO,[5]
CARMELLE ROBERT,[6] AND WALLACE L. W. SARGENT[7]

Received 1995 September 29; accepted 1996 February 19

ABSTRACT

We have obtained an *HST Faint Object Camera* ultraviolet image and *Faint Object Spectrograph* ultraviolet spectra of the central starburst region in the nearby amorphous galaxy NGC 4214. The ultraviolet image reveals a bright, compact, starburst knot surrounded by more than 200 fainter pointlike sources. Spectral synthesis modeling of the ultraviolet spectrum of the central starburst knot suggests the stellar population has an age of 4–5 Myr. The extinction-corrected ultraviolet flux implies that hundreds of O-type stars are contained within a diameter of at most 5 pc. The inferred number of Wolf-Rayet (W-R) stars implies that the star formation episode occurred in a short duration burst. The starburst knot contains roughly twice the number of O stars as in a similar size region centered on R136a in 30 Doradus, but it is slightly older. The knot in NGC 4214 is comparable in size and luminosity to the starburst knots identified in the core of the W-R galaxy He 2–10 and to the super star clusters found in other star-forming galaxies. The number of Lyman continuum photons inferred from Hα measurements is at least a factor of 4 smaller than that predicted from the observed numbers of hot stars; this starburst knot is thus "density bounded" to ionizing radiation. The fainter pointlike sources seen in the ultraviolet image are probably individual hot stars or small groups of stars. The ultraviolet luminosity function of these objects is similar to that found for stars within 30 Doradus.

Subject headings: galaxies: individual (NGC 4214) — galaxies: starburst — galaxies: stellar content — ultraviolet: galaxies

1. INTRODUCTION

NGC 4214 is a nearby, relatively gas-rich Magellanic Irregular galaxy with very blue colors ($B_T \approx 10.2$ mag, $(B-V)_T \approx 0.5$; Sandage & Bedke 1988, 1994; de Vaucouleurs et al. 1991). At a distance of approximately 4.1 Mpc,[8] the absolute blue magnitude of the galaxy is $M^0{}_B \approx -18.8$ mag. Classified as SBmIII by Sandage & Bedke (1988, 1994) and as IAB(s)m by de Vaucouleurs et al. (1991), NGC 4214 contains an amorphous central part, with indications of faint spiral arms. This galaxy has been studied in a number of different wavelength regions. Hunter (1982) presented Hα images of NGC 4214 and discussed the physical properties of the H II regions in the central amorphous region. The H II regions in NGC 4214 are luminous but not exceptional as compared to H II regions in other irregular galaxies (Sargent & Filippenko 1991, hereafter SF91).

Huchra et al. (1983) studied the star formation history of NGC 4214 using *International Ultraviolet Explorer* (*IUE*) spectroscopy, and optical and infrared imaging, and suggested that the galaxy experienced a burst of star formation a few $\times 10^7$ yr ago, when a few percent of the present stellar mass was formed. Noting that the gas in NGC 4214 had a complicated velocity field, Hartmann, Geller, & Huchra (1986) linked the recent starburst to a possible recent merger with another gas-rich galaxy. Thronson et al. (1988) used near- and far-infrared continuum and CO emission line observations to study the star formation properties of the galaxy and suggested a current rate of star formation of 0.5–1 $M_\odot$ yr^{-1}.

Observations by SF91 revealed the presence of a broad emission feature near 4660 Å in the optical spectra of two bright knots in the central regions of NGC 4214. This broad feature in integrated spectra, due primarily to He II λ4686 emission, is the defining characteristic of a subset of starburst galaxies known as Wolf-Rayet (W-R) galaxies and indicates the presence of W-R stars (e.g., Kunth & Joubert 1985; Conti 1991). The analysis by SF91 suggested that roughly *equal* numbers of W-R and O-type stars are present in these knots. This result is surprising, given the belief that W-R stars are the short-lived He-burning descendents of the most massive stars (e.g., Maeder & Conti 1994). In general, the lifetime of W-R stars is only about 10% of the H-burning lifetime of their progenitors, and therefore the

---

[1] Based on observations with the NASA/ESA *Hubble Space Telescope*, obtained at the Space Telescope Science Institute, which is operated by AURA, Inc., for NASA under contract NAS5-26555.

[2] Space Telescope Science Institute, 3700 San Martin Drive, Baltimore, MD 21218; leitherer@stsci.edu.

[3] Institute for Astronomy, 2680 Woodlawn Drive, Honolulu, HI 96822; vacca@athena.ifa.hawaii.edu.

[4] JILA, University of Colorado, Boulder, CO 80309-0440; pconti@jila.colorado.edu.

[5] Department of Astronomy, University of California, Berkeley, CA 94720-3411; alex@astro.berkeley.edu.

[6] Space Telescope Science Institute, 3700 San Martin Drive, Baltimore, MD 21218; currently at University of Laval, Department of Physics, Quebec, G1K 7P4 Canada; carobert@phy.ulaval.ca.

[7] Astronomy Department, 105-24, California Institute of Technology, Pasadena, CA 91125; wws@deimos.caltech.edu.

[8] The observed Galactocentric velocity of NGC 4214 is 313 km s^{-1} (de Vaucouleurs et al. 1991). Using the linear Virgocentric infall model of Schechter (1980), the velocity of the Virgo cluster corrected to the centroid of the Local Group (976 km s^{-1}) and the infall velocity of the Local Group toward Virgo (220 km s^{-1}) given by Binggeli et al. (1987), and the distance to the Virgo cluster (17.6 Mpc) given by Jacoby et al. (1992), we find the distance to NGC 4214 is 4.1 Mpc. Other values of the velocity and distance to the Virgo cluster generally lead to smaller distances for NGC 4214. Alternatively, NGC 4214 is a member of the Canes Venatici I cloud of galaxies, for which Rowan-Robinson (1985, p. 210) estimated a distance of 5.1 Mpc using the results from a number of different distance determination methods. Recently, Saha et al. (1994) detected Cepheids in IC 4182, another member of the Canes Venatici I cloud, and derived a distance of 4.7 Mpc to this galaxy. Our estimate of the distance to NGC 4214 is intermediate between these various values.

number ratio of W-R to O stars is expected to be about 0.1 in solar abundance regions experiencing continuous star formation (Maeder 1991). SF91 suggested that the high number ratios found in the knots were the result of an intense burst of star formation, with a duration of less than 10^6 yr, which occurred less than 5 Myr ago. It is also possible that the upper mass end of the initial mass function (IMF) in the knots is flat, or "top heavy" with massive stars. An alternative explanation for the high number ratio is that the regions of the knots included in the spectroscopic observations are not ionization bounded. If they are density bounded, a large percentage of the ionizing photons escape the region, and the observed flux in the Balmer lines yields an underestimate of the number of O stars present.

We chose to observe the brightest starburst knot in NGC 4214 with the *Hubble Space Telescope* (*HST*), because it is one of the nearest W-R galaxies and because the inferred ratio of W-R to O-type stars is inordinately large compared to both observations of other W-R galaxies (see Vacca & Conti 1992) and theoretical expectations of starbursts (Maeder & Meynet 1994). We obtained an ultraviolet (UV) image with the Faint Object Camera (FOC) and UV spectra with the Faint Object Spectrograph (FOS) as discussed in § 2. The overall UV spatial morphology is discussed in § 3. We use the measured UV flux in the starburst knot to estimate the numbers of hot stars contained within it. We also detect other luminous objects in the field surrounding the starburst knot, which we suggest are individual hot stars or small clusters of stars. A spectral synthesis analysis of the UV spectrum of the starburst knot is used (§ 4) to infer its age, the duration of the starburst episode, and the numbers of hot stars present. These direct measures of the hot star population are then compared with those inferred from the ionized gas and the Hα recombination lines in a reanalysis of the optical data (§ 5). In § 6, the bright starburst knot in NGC 4214 is contrasted with the 30 Doradus region in the Large Magellanic Cloud (LMC). We draw some general conclusions about the analyses and the nature of starburst phenomena in § 7.

2. OBSERVATIONS

2.1. *HST FOC Ultraviolet Imaging*

An image of NGC 4214 was obtained with the FOC on board the *HST* on 1993 March 3 UT. The observation was made in the f/96 configuration, in the "zoomed" format, with the F220W (effective wavelength of ∼2200 Å) and F2ND (neutral density) filters. The total exposure time was 1196.75 s. The original image format consisted of 512×1024 pixels and had a field of view of $\sim 22'' \times 22''$. In this format, the dynamic range is limited to 8 bits per pixel, which restricts the total count value within any pixel to the range 0–255, modulo 255. It was found that a number of pixels within the bright central object in the image had "rolled over" the maximum value of 255. We corrected the counts in these pixels by manually adding 255. However, the count rates in these pixels were high enough that this portion of the image suffered from substantial detector nonlinearity and the true counts in these pixels cannot be very accurately determined. The corrected image was then processed with the standard *HST* data reduction pipeline, which involved "rebinning" the pixels in order to produce a square image format, correcting the image for geometric distortion, and dividing by a flat-field image. In addition, we removed the reseau marks from the image by interpolating over them. We then corrected for large-scale (i.e., spatial scales ≥10 pixels) spatially dependent nonlinearity using the algorithms given by Jedrzejewski (1992) and Baxter (1993a). Over most of the image (excluding the central object) this correction amounts to an increase in flux of less than about 10%. The final image, rotated so that north is up and east is to the left, is shown in Figure 1. The scale for this image is $0\farcs022497$ pixel^{-1} (Baxter 1993b); at a distance of 4.1 Mpc, this corresponds to 0.45 pc pixel^{-1}, or 20 pc arcsec^{-1}.

2.2. *HST FOS Spectroscopy*

FOS spectra of the bright starburst knot of NGC 4214 were obtained on 1993 November 1 UT using gratings G130H and G190H, both on the FOS blue side, with exposure times of 1900 and 1000 s, respectively. The total wavelength range covered by the two gratings is 1200–2300 Å. Despite the reduced sensitivity at the longest wavelengths in comparison to a red side observation with G190H, the blue side observations with G190H allowed us to avoid a side-switch that would have introduced an additional positional uncertainty. In addition, we are particularly interested in the wavelength region around He II λ1640, where the red and blue sides have comparable sensitivity for G190H.

The target acquisition strategy was devised based on our previously acquired FOC image. The starburst region appeared extended under the pre-COSTAR observing conditions, but a standard, direct on-board acquisition could still be carried out. An initial peak-up into the $4\farcs3$ aperture was done, followed by two additional peak-ups into the circular $1\farcs0$ and $0\farcs5$ apertures. The science exposures with the two gratings were done with the $1\farcs0$ circular aperture. The final *HST* pointing, as determined from the engineering data stream, was R.A. = $12^{\rm h}15^{\rm m}39\fs41$ and decl. = $+36°19'36\farcs0$ (J2000). The region of NGC 4214 within the FOS aperture is the bright central knot seen in the FOC image and corresponds to knot 1 in the nomenclature of SF91. We will refer to this region as NGC 4214-1. NGC 4214-1 is one of several star-forming regions in NGC 4214 (Hunter 1982; SF91) but it is not the most prominent region in terms of its Hα luminosity (see the discussion in § 5.1). It was selected for observation with the FOS because of the presence of Wolf-Rayet stars.

The data were reduced with the standard pipeline reduction software found in the STSDAS package in IRAF.[9] The signal in those diodes located in wavelength regions with no sensitivity to the dispersed light (because of optical cutoffs) was used to determine the scattered light component. We found no significant contamination, as expected from the blue color of NGC 4214-1. The data reduction was performed before the revised absolute flux calibration for the FOS (Bohlin 1993) had been implemented in the standard pipeline reduction. We applied a correction manually by dividing the NGC 4214-1 spectrum by a function representing the ratio of the old to the new sensitivity. Therefore, the spectra presented in this paper are on the new theoretical flux scale, which is tied to a model atmosphere for the white dwarf G191B2B. The new flux scale is

---

[9] IRAF (Image Reduction and Analysis Facility) is distributed by the National Optical Astronomy Observatories, which are operated by AURA, Inc., under cooperative agreement with the National Science Foundation.

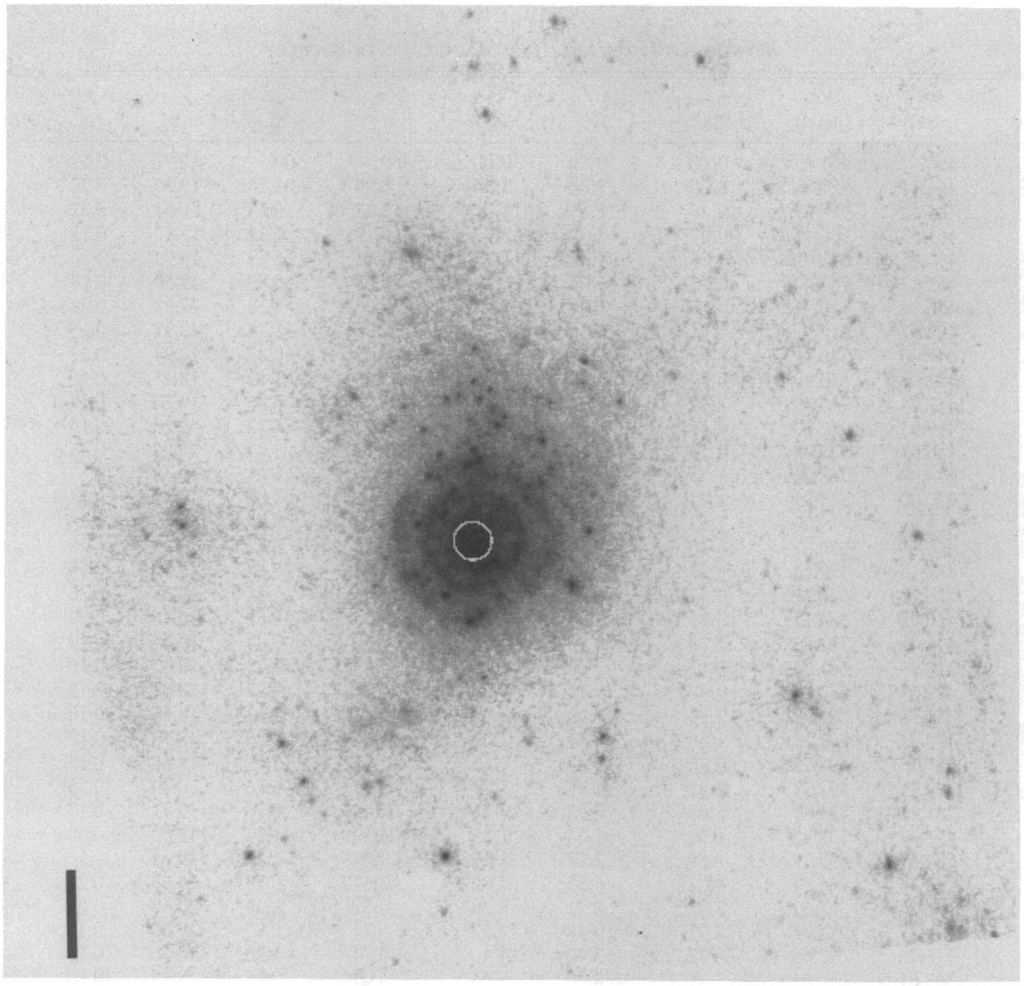

FIG. 1.—Ultraviolet (2200 Å) image of NGC 4214-1 observed with the FOC, displayed on a logarithmic intensity scale. The image is ~22″ × 22″; the plate scale is 0″.022497 pixel^{-1}. A bar representing 2″ is in the lower left corner. The circle denotes the location of the FOS aperture. This image was produced from the original by following the procedure outlined in the text and then by rotating so that north is up and east is to the left. The central object has approximate pixel coordinates (456, 461) and J2000 coordinates 12^{h}15^{m}39^s.41, 36°19′36″.0 with an uncertainty of about 0″.5.

particularly relevant for the spectral regions around the Si IV λ1400 and C IV λ1550 lines, which would otherwise be affected by broad dips with amplitudes of up to 10% of the continuum level.

The original spectra were oversampled by quarter-diode subpixel steps. In order to increase the signal-to-noise (S/N) ratio, we smoothed the data by applying a boxcar filter over four pixels. We measured the widths of the Lyman-α geocoronal line and of unblended interstellar lines to determine the actual spectral resolution. Lyman-α has full width at half-maximum (FWHM) of 2.2 Å, and the interstellar lines have an average FWHM of 2.5 Å. These values are close to the nominal line widths if the illuminating source fills the aperture uniformly (see FOS Instrument Handbook Version 6.0, Table 1-5). This suggests that the starburst as observed pre-COSTAR is significantly more extended than a point source. In the FOC image (§ 3), on the other hand, NGC 4214-1 appears consistent with a point source, with a formal limit of FWHM $\lesssim$ 0″.2. Moreover, the only other sources within the 1″ FOS aperture are much fainter than NGC 4214-1. [The source north of NGC 4214-1 is resolved into two faint peaks (146 and 148 in Table 1), while the source south of NGC 4214-1 (128) does not show such structure. These sources are too faint and too close to NGC 4214-1 to be recognizable in Fig. 1.] Perhaps macroscopic motions and turbulence in the interstellar medium account for most of the broadening of the interstellar lines.

No simultaneous wavelength calibration with the internal calibration lamp was obtained during the observations. The dominant error in the zero point of the wavelength scale is the nonrepeatability in the positioning of the filter-grating wheel, of the order of 0.3 diodes. We verified the consistency between this value and our observations by measuring the positions of the Lyman-α geocoronal line and of unblended interstellar lines. The Lyman-α geocoronal line has a geocentric velocity of +90 km s^{-1}. The mean velocity (in the rest frame of NGC 4214) of Si II λ1260, O I/Si II λ1300, C II λ1335, Si II λ1526, and Al II λ1670 is +30 km s^{-1}. These values are well within the expected uncertainty and are consistent with the assumption of no significant wavelength offset.

3. IMAGE PROPERTIES OF NGC 4214

3.1. *Reduction of the Ultraviolet Image*

Figure 1 reveals that NGC 4214 consists of a bright central object (NGC 4214-1) surrounded by a large number of fainter pointlike sources. NGC 4214-1 corresponds to knot 1 of SF91; knots 2 and 3 of SF91 were not contained within the FOC field of view (knot 1 is not quite centered),

TABLE 1

Positions, Fluxes, and *HST* Magnitudes of Sources

Number	X[a] (pixel)	Y[a] (pixel)	$\Delta\alpha$[b]	$\Delta\delta$[b]	r[b]	Flux[c]	σ[c]	m_{2200}	σ	M_{2200}
1......	456	461	0″.00	0″.00	0″.00	2460	500	12.92	0.22	−15.86
2......	464.74	587.00	0.04	2.84	2.84	6.94	1.26	19.30	0.20	−9.48
3......	484.41	951.29	0.26	11.05	11.05	2.27	0.67	20.51	0.32	−8.27
4......	461.63	566.41	0.07	2.37	2.37	8.19	1.38	19.12	0.18	−9.66
5......	457.15	521.00	0.08	1.35	1.35	9.76	1.79	18.93	0.20	−9.85
6......	461.17	757.40	0.43	6.66	6.67	5.28	0.89	19.59	0.18	−9.19
7......	456.54	539.71	0.13	1.77	1.77	32.33	2.28	17.63	0.08	−11.15
8......	454.67	612.31	0.31	3.39	3.40	9.95	1.36	18.91	0.15	−9.87
9......	447.00	746.00	0.73	6.37	6.41	3.85	0.82	19.94	0.23	−8.84
10......	442.03	610.90	0.59	3.34	3.39	15.68	1.52	18.41	0.10	−10.37
11......	417.24	790.36	1.47	7.31	7.46	4.78	0.85	19.70	0.19	−9.08
12......	419.93	763.00	1.36	6.71	6.84	7.37	1.12	19.23	0.16	−9.55
13......	440.53	578.98	0.56	2.62	2.68	3.36	1.07	20.08	0.35	−8.70
14......	414.00	768.00	1.51	6.81	6.97	6.45	1.01	19.38	0.17	−9.40
15......	427.00	661.83	1.02	4.45	4.56	6.36	1.05	19.39	0.18	−9.39
16......	409.41	719.00	1.52	5.70	5.90	4.09	0.85	19.87	0.23	−8.91
17......	356.81	936.07	3.10	10.47	10.92	4.26	0.72	19.83	0.18	−8.95
18......	329.18	999.44	3.83	11.84	12.44	5.67	0.83	19.52	0.16	−9.26
19......	436.15	538.89	0.59	1.71	1.81	6.45	1.54	19.38	0.26	−9.40
20......	430.25	554.13	0.75	2.04	2.17	19.75	1.65	18.16	0.09	−10.62
21......	377.45	742.83	2.28	6.17	6.58	4.76	0.84	19.71	0.19	−9.07
22......	415.93	581.35	1.12	2.62	2.85	16.29	1.48	18.37	0.10	−10.41
23......	438.59	512.00	0.48	1.11	1.21	20.85	2.22	18.10	0.12	−10.68
24......	331.38	782.98	3.39	6.99	7.77	12.44	1.17	18.66	0.10	−10.12
25......	397.49	607.13	1.58	3.17	3.54	11.74	1.26	18.73	0.12	−10.05
26......	427.58	528.78	0.76	1.47	1.65	12.52	1.69	18.66	0.15	−10.12
27......	349.71	691.29	2.81	4.97	5.71	3.33	0.76	20.09	0.25	−8.69
28......	261.83	831.49	5.03	7.95	9.41	4.73	0.76	19.71	0.17	−9.07
29......	417.43	532.82	1.00	1.54	1.83	22.50	1.84	18.02	0.09	−10.76
30......	384.61	592.79	1.84	2.82	3.37	7.47	1.13	19.22	0.16	−9.56
31......	288.44	765.74	4.32	6.52	7.82	3.67	0.73	19.99	0.22	−8.79
32......	376.24	588.52	2.02	2.71	3.38	4.87	0.96	19.68	0.21	−9.10
33......	149.27	948.93	7.77	10.38	12.97	5.77	0.87	19.50	0.16	−9.28
34......	345.74	622.65	2.77	3.42	4.40	13.74	1.30	18.56	0.10	−10.22
35......	303.61	660.61	3.78	4.20	5.65	4.07	0.75	19.88	0.20	−8.90
36......	429.50	492.96	0.65	0.67	0.93	26.09	2.27	17.86	0.09	−10.92
37......	356.00	574.21	2.45	2.35	3.40	4.25	0.85	19.83	0.22	−8.95
38......	358.12	570.60	2.40	2.28	3.31	4.32	0.89	19.81	0.22	−8.97
39......	329.63	602.00	3.09	2.93	4.26	7.13	1.04	19.27	0.16	−9.51
40......	278.00	648.27	4.34	3.87	5.81	4.15	0.78	19.86	0.20	−8.92
41......	179.34	671.00	6.59	4.20	7.81	3.55	0.75	20.02	0.23	−8.76
42......	158.13	609.35	6.95	2.78	7.49	3.45	0.74	20.06	0.23	−8.72
43......	399.82	483.99	1.30	0.41	1.37	44.27	2.33	17.28	0.06	−11.50
44......	324.58	504.00	3.03	0.72	3.11	5.02	0.88	19.65	0.19	−9.13
45......	62.00	574.48	9.04	1.82	9.22	4.20	0.77	19.84	0.20	−8.94
46......	155.40	525.01	6.86	0.88	6.91	21.03	1.57	18.09	0.08	−10.69
47......	238.47	498.93	4.95	0.45	4.97	4.41	0.83	19.79	0.20	−8.99
48......	148.00	510.46	7.00	0.54	7.02	7.46	1.08	19.22	0.16	−9.56
49......	66.75	521.07	8.84	0.63	8.86	5.42	0.87	19.56	0.17	−9.22
50......	155.47	504.98	6.82	0.43	6.83	21.98	1.57	18.04	0.08	−10.74
51......	114.00	505.00	7.75	0.36	7.76	3.90	0.83	19.92	0.23	−8.86
52......	117.38	498.19	7.66	0.21	7.66	9.76	1.12	18.93	0.12	−9.85
53......	165.48	492.00	6.57	0.16	6.57	3.77	0.86	19.96	0.25	−8.82
54......	162.93	473.53	6.59	−0.26	6.60	7.97	1.02	19.15	0.14	−9.63
55......	132.00	460.00	7.26	−0.62	7.29	4.96	0.85	19.66	0.19	−9.12
56......	66.64	436.49	8.69	−1.27	8.78	4.75	0.85	19.71	0.19	−9.07
57......	362.34	452.58	2.08	−0.36	2.12	6.68	1.13	19.34	0.18	−9.44
58......	273.00	431.00	4.05	−1.01	4.17	4.06	0.76	19.88	0.20	−8.90
59......	164.75	406.98	6.43	−1.75	6.66	6.06	0.88	19.44	0.16	−9.34
60......	348.69	424.38	2.34	−1.02	2.55	7.15	1.07	19.26	0.16	−9.52
61......	405.19	442.40	1.11	−0.51	1.22	13.92	1.66	18.54	0.13	−10.24
62......	393.40	432.14	1.35	−0.76	1.55	24.56	2.01	17.92	0.09	−10.86
63......	405.59	426.17	1.07	−0.87	1.38	16.12	1.77	18.38	0.12	−10.40
64......	400.13	420.43	1.18	−1.01	1.55	14.50	1.69	18.50	0.13	−10.28
65......	226.40	281.40	4.82	−4.45	6.56	4.30	0.81	19.82	0.20	−8.96
66......	237.74	271.38	4.55	−4.65	6.50	22.01	1.54	18.04	0.08	−10.74
67......	276.13	299.32	3.74	−3.96	5.44	4.53	0.85	19.76	0.20	−9.02
68......	83.60	93.36	7.67	−8.93	11.77	3.23	0.73	20.13	0.24	−8.65
69......	138.06	118.43	6.50	−8.27	10.51	6.08	0.85	19.44	0.15	−9.34
70......	381.13	378.90	1.53	−1.98	2.50	6.42	1.12	19.38	0.19	−9.40
71......	193.34	159.30	5.33	−7.25	9.00	28.33	1.70	17.77	0.06	−11.01
72......	256.40	230.27	4.05	−5.54	6.86	19.86	1.46	18.16	0.08	−10.62

TABLE 1—*Continued*

Number	X^a (pixel)	Y^a (pixel)	$\Delta\alpha^b$	$\Delta\delta^b$	r^b	Flux^c	σ^c	m_{2200}	σ	M_{2200}
73......	306.00	269.75	3.01	−4.56	5.47	3.57	0.82	20.02	0.25	−8.76
74......	230.85	172.49	4.52	−6.88	8.23	6.29	0.88	19.40	0.15	−9.38
75......	263.43	210.68	3.86	−5.97	7.11	5.80	0.91	19.49	0.17	−9.29
76......	322.20	281.77	2.67	−4.26	5.03	3.62	0.88	20.00	0.26	−8.78
77......	274.86	194.06	3.57	−6.32	7.26	4.93	0.84	19.67	0.18	−9.11
78......	422.31	408.06	0.66	−1.25	1.41	52.94	2.57	17.09	0.05	−11.69
79......	323.52	236.15	2.56	−5.29	5.87	4.42	0.88	19.79	0.22	−8.99
80......	425.82	407.26	0.58	−1.26	1.39	22.91	1.95	18.00	0.09	−10.78
81......	321.22	219.92	2.58	−5.65	6.21	8.55	1.08	19.07	0.14	−9.71
82......	352.20	267.84	1.97	−4.52	4.93	2.79	0.87	20.29	0.34	−8.49
83......	370.24	291.23	1.61	−3.96	4.28	5.55	1.07	19.54	0.21	−9.24
84......	335.68	222.76	2.26	−5.56	6.00	7.12	1.02	19.27	0.16	−9.51
85......	377.90	251.94	1.37	−4.83	5.02	3.50	0.82	20.04	0.25	−8.74
86......	403.39	302.78	0.89	−3.64	3.75	4.43	0.89	19.78	0.22	−9.00
87......	335.43	33.56	1.92	−9.81	9.99	6.97	0.91	19.29	0.14	−9.49
88......	427.01	346.27	0.44	−2.63	2.66	4.91	0.98	19.67	0.22	−9.11
89......	428.82	320.56	0.35	−3.20	3.22	7.81	1.07	19.17	0.15	−9.61
90......	397.17	139.23	0.73	−7.32	7.36	56.33	2.38	17.02	0.05	−11.76
91......	389.94	81.43	0.78	−8.63	8.67	7.10	0.93	19.27	0.14	−9.51
92......	446.02	378.30	0.07	−1.87	1.87	25.88	2.05	17.87	0.09	−10.91
93......	440.13	285.16	0.03	−3.97	3.97	4.50	0.85	19.77	0.21	−9.01
94......	453.38	318.63	−0.20	−3.20	3.20	9.67	1.13	18.94	0.13	−9.84
95......	454.02	195.45	−0.44	−5.96	5.97	4.93	0.82	19.67	0.18	−9.11
96......	457.28	385.66	−0.17	−1.69	1.70	38.10	2.28	17.45	0.07	−11.33
97......	494.33	248.74	−1.25	−4.69	4.85	6.66	0.93	19.34	0.15	−9.44
98......	494.86	268.59	−1.23	−4.24	4.42	3.80	0.81	19.95	0.23	−8.83
99......	494.86	268.59	−1.23	−4.24	4.42	3.80	0.81	19.95	0.23	−8.83
100......	476.73	401.66	−0.57	−1.29	1.41	11.87	1.65	18.71	0.15	−10.07
101......	480.67	402.83	−0.66	−1.26	1.42	10.23	1.59	18.88	0.17	−9.90
102......	569.80	224.53	−2.99	−5.09	5.90	13.32	1.25	18.59	0.10	−10.19
103......	649.08	67.34	−5.05	−8.47	9.86	5.95	0.86	19.46	0.16	−9.32
104......	573.00	247.60	−3.02	−4.57	5.48	24.57	1.63	17.92	0.07	−10.86
105......	472.46	435.95	−0.42	−0.53	0.67	36.21	2.71	17.50	0.08	−11.28
106......	589.28	272.23	−3.34	−3.99	5.20	7.39	0.94	19.23	0.14	−9.55
107......	532.49	354.00	−1.91	−2.26	2.96	3.13	0.86	20.16	0.30	−8.62
108......	820.24	62.23	−8.90	−8.27	12.15	4.36	0.81	19.80	0.20	−8.98
109......	713.00	193.14	−6.25	−5.53	8.35	3.31	0.69	20.10	0.23	−8.68
110......	477.74	438.54	−0.53	−0.46	0.70	37.92	2.69	17.45	0.08	−11.33
111......	916.35	13.92	−11.14	−9.18	14.44	8.24	1.13	19.11	0.15	−9.67
112......	913.23	33.80	−11.04	−8.74	14.08	4.61	0.86	19.74	0.20	−9.04
113......	858.80	85.98	−9.72	−7.67	12.38	23.97	1.64	17.95	0.07	−10.83
114......	857.37	92.62	−9.68	−7.52	12.26	13.23	1.26	18.60	0.10	−10.18
115......	930.52	42.00	−11.41	−8.52	14.24	5.21	0.94	19.61	0.20	−9.17
116......	954.39	28.33	−11.97	−8.78	14.85	4.44	0.83	19.78	0.20	−9.00
117......	747.09	235.00	−6.94	−4.53	8.29	3.80	0.75	19.95	0.21	−8.83
118......	879.28	142.00	−10.08	−6.37	11.92	2.80	0.73	20.28	0.28	−8.5
119......	818.40	191.03	−8.62	−5.39	10.17	3.35	0.76	20.09	0.25	−8.69
120......	824.71	191.73	−8.76	−5.36	10.27	5.83	0.87	19.49	0.16	−9.29
121......	926.42	155.87	−11.11	−5.98	12.61	10.95	1.14	18.80	0.11	−9.98
122......	792.51	255.26	−7.92	−3.99	8.87	6.21	0.97	19.42	0.17	−9.36
123......	930.57	178.19	−11.16	−5.47	12.43	10.75	1.13	18.82	0.11	−9.96
124......	777.23	270.76	−7.55	−3.67	8.40	21.82	1.56	18.05	0.08	−10.73
125......	896.91	200.55	−10.36	−5.03	11.52	3.28	0.74	20.11	0.25	−8.67
126......	578.81	391.39	−2.88	−1.33	3.18	4.83	0.97	19.69	0.22	−9.09
127......	555.04	406.36	−2.32	−1.04	2.54	31.90	2.04	17.64	0.07	−11.14
128......	465.41	455.89	−0.22	−0.10	0.24	101.94	4.29	16.38	0.05	−12.4
129......	500.13	442.86	−1.02	−0.33	1.07	21.95	2.16	18.05	0.11	−10.73
130......	671.76	378.20	−4.99	−1.46	5.20	4.37	0.80	19.80	0.20	−8.98
131......	903.00	307.36	−10.31	−2.62	10.63	4.10	0.76	19.87	0.20	−8.91
132......	544.56	437.93	−2.03	−0.35	2.06	10.14	1.39	18.88	0.15	−9.90
133......	765.22	382.22	−7.08	−1.20	7.18	3.08	0.70	20.18	0.25	−8.60
134......	816.84	377.35	−8.24	−1.21	8.33	4.26	0.79	19.83	0.20	−8.95
135......	904.86	362.98	−10.24	−1.37	10.34	3.12	0.73	20.16	0.25	−8.62
136......	757.31	397.26	−6.87	−0.88	6.93	3.13	0.71	20.16	0.25	−8.62
137......	919.95	423.71	−10.47	0.02	10.47	12.65	1.20	18.65	0.10	−10.13
138......	577.93	460.29	−2.74	0.21	2.74	26.84	1.80	17.83	0.07	−10.95
139......	672.00	497.47	−4.78	1.21	4.93	4.18	0.78	19.85	0.20	−8.93
140......	860.25	533.54	−8.93	2.37	9.24	15.41	1.31	18.43	0.09	−10.35
141......	769.84	529.00	−6.91	2.10	7.22	3.14	0.69	20.16	0.24	−8.62
142......	922.19	579.77	−10.23	3.52	10.82	2.56	0.68	20.38	0.29	−8.40
143......	554.86	489.00	−2.17	0.81	2.31	7.91	1.29	19.15	0.18	−9.63
144......	584.15	498.00	−2.81	1.07	3.00	4.60	1.08	19.74	0.25	−9.04
145......	605.32	504.31	−3.27	1.25	3.50	5.13	0.99	19.62	0.21	−9.16

TABLE 1—*Continued*

Number	X^{a} (pixel)	Y^{a} (pixel)	$\Delta\alpha^{b}$	$\Delta\delta^{b}$	r^{b}	Flux^{c}	σ^{c}	m_{2200}	σ	M_{2200}
146	466.00	464.00	−0.22	0.09	0.23	81.26	3.96	16.63	0.05	−12.15
147	869.46	607.00	−9.00	4.03	9.86	2.82	0.70	20.27	0.27	−8.51
148	467.64	465.47	−0.25	0.12	0.28	81.28	3.78	16.63	0.05	−12.15
149	792.99	600.80	−7.30	3.75	8.21	8.32	1.03	19.10	0.13	−9.68
150	874.47	651.31	−9.03	5.04	10.34	5.68	0.86	19.51	0.16	−9.27
151	583.20	538.27	−2.71	1.97	3.35	7.12	1.08	19.27	0.16	−9.51
152	859.70	713.51	−8.59	6.40	10.71	3.43	0.75	20.06	0.24	−8.72
153	809.86	689.00	−7.51	5.76	9.47	4.13	0.79	19.86	0.21	−8.92
154	565.78	532.46	−2.33	1.80	2.95	5.71	1.16	19.51	0.22	−9.27
155	792.97	681.12	−7.15	5.56	9.05	3.04	0.74	20.19	0.26	−8.59
156	515.36	499.88	−1.26	0.98	1.60	20.79	1.93	18.11	0.10	−10.67
157	681.73	610.73	−4.79	3.77	6.09	3.83	0.82	19.94	0.23	−8.84
158	503.00	493.12	−0.99	0.81	1.28	15.05	1.81	18.46	0.13	−10.32
159	532.71	514.24	−1.62	1.33	2.10	22.05	1.81	18.04	0.09	−10.74
160	823.36	735.22	−7.73	6.82	10.31	3.05	0.73	20.19	0.26	−8.59
161	544.64	528.21	−1.86	1.67	2.50	12.28	1.46	18.68	0.13	−10.10
162	622.13	591.16	−3.49	3.22	4.75	13.21	1.28	18.60	0.11	−10.18
163	723.82	672.30	−5.62	5.23	7.67	3.42	0.79	20.07	0.25	−8.71
164	519.33	512.10	−1.33	1.26	1.83	11.54	1.67	18.74	0.16	−10.04
165	671.00	636.00	−4.50	4.32	6.24	3.23	0.74	20.13	0.25	−8.65
166	741.31	727.90	−5.91	6.51	8.79	3.59	0.74	20.01	0.22	−8.77
167	679.49	676.82	−4.61	5.25	6.99	3.33	0.76	20.09	0.25	−8.69
168	593.88	596.72	−2.84	3.30	4.35	4.81	0.96	19.69	0.22	−9.09
169	692.99	701.81	−4.87	5.84	7.60	4.06	0.77	19.88	0.21	−8.90
170	586.35	613.94	−2.64	3.67	4.52	9.07	1.18	19.01	0.14	−9.77
171	538.01	558.25	−1.66	2.33	2.86	27.86	1.88	17.79	0.07	−10.99
172	599.59	631.54	−2.91	4.09	5.02	4.01	0.90	19.89	0.24	−8.89
173	489.45	502.16	−0.67	0.98	1.19	12.70	1.89	18.64	0.16	−10.14
174	692.06	760.80	−4.74	7.16	8.58	5.04	0.83	19.64	0.18	−9.14
175	589.92	635.86	−2.68	4.17	4.95	22.64	1.58	18.01	0.08	−10.77
176	643.88	712.45	−3.75	5.98	7.06	3.83	0.77	19.94	0.22	−8.84
177	525.58	561.62	−1.38	2.38	2.75	8.73	1.37	19.05	0.17	−9.73
178	549.42	596.79	−1.84	3.22	3.71	11.82	1.33	18.72	0.12	−10.06
179	505.39	537.91	−0.97	1.82	2.06	10.49	1.49	18.85	0.15	−9.93
180	740.06	935.73	−5.50	11.17	12.45	18.95	1.42	18.21	0.08	−10.57
181	536.91	603.58	−1.55	3.35	3.69	6.06	1.14	19.44	0.20	−9.34
182	701.56	912.07	−4.68	10.57	11.55	3.82	0.75	19.94	0.21	−8.84
183	595.00	743.33	−2.60	6.59	7.08	4.88	0.88	19.68	0.19	−9.10
184	593.15	751.51	−2.54	6.77	7.23	7.29	1.00	19.24	0.15	−9.54
185	485.15	526.12	−0.53	1.51	1.61	14.67	1.78	18.48	0.13	−10.3
186	523.57	612.00	−1.24	3.51	3.72	4.35	1.07	19.80	0.27	−8.98
187	557.63	713.44	−1.81	5.85	6.12	4.63	0.86	19.74	0.20	−9.04
188	647.18	944.18	−3.40	11.19	11.69	4.44	0.78	19.78	0.19	−9.00
189	525.80	658.35	−1.20	4.55	4.71	6.58	1.06	19.35	0.18	−9.43
190	500.38	586.56	−0.76	2.90	3.00	15.01	1.57	18.46	0.11	−10.32
191	486.49	547.31	−0.52	1.99	2.06	7.21	1.40	19.25	0.21	−9.53
192	612.30	948.44	−2.61	11.22	11.52	3.92	0.78	19.92	0.21	−8.86
193	492.71	578.35	−0.61	2.70	2.77	24.93	1.85	17.91	0.08	−10.87
194	600.66	988.45	−2.27	12.09	12.30	5.38	0.87	19.57	0.18	−9.21
195	591.19	990.19	−2.06	12.11	12.29	12.06	1.19	18.70	0.11	−10.08
196	489.00	595.68	−0.49	3.08	3.12	8.60	1.38	19.06	0.17	−9.72
197	481.56	571.26	−0.37	2.52	2.55	6.87	1.34	19.31	0.21	−9.47
198	488.75	615.77	−0.45	3.53	3.56	15.11	1.49	18.45	0.11	−10.33
199	489.56	636.94	−0.43	4.01	4.03	6.48	1.12	19.37	0.19	−9.41
200	544.00	951.11	−1.07	11.15	11.20	8.42	1.00	19.09	0.13	−9.69
201	470.28	545.33	−0.17	1.92	1.92	24.50	2.09	17.93	0.09	−10.85
202	472.53	568.85	−0.17	2.45	2.45	6.31	1.33	19.40	0.23	−9.38
203	477.39	608.30	−0.21	3.34	3.35	18.03	1.60	18.26	0.10	−10.52
204	510.45	900.70	−0.41	9.96	9.97	15.74	1.32	18.41	0.09	−10.37
205	465.55	554.89	−0.04	2.12	2.12	28.87	2.03	17.75	0.08	−11.03
206	505.48	952.00	−0.21	11.10	11.10	4.09	0.82	19.87	0.22	−8.91
207	475.96	659.93	−0.08	4.50	4.50	13.30	1.35	18.59	0.11	−10.19
208	464.09	542.44	−0.03	1.84	1.84	10.45	1.91	18.85	0.20	−9.93
209	482.70	742.77	−0.08	6.37	6.37	5.91	0.93	19.47	0.17	−9.31
210	471.55	626.20	−0.04	3.73	3.73	14.52	1.47	18.49	0.11	−10.29
211	478.87	710.75	−0.05	5.64	5.64	5.77	0.97	19.50	0.18	−9.28
212	500.00	952.00	−0.08	11.09	11.09	6.50	0.94	19.37	0.16	−9.41
213+	504.39	1005.67	−0.08	12.30	12.30	8.08	0.95	19.13	0.13	−9.65

---

[a] Pixels measured from the lower left corner of the original image.

[b] Relative location of knot in R.A. and decl. and distance in arcsec with respect to NGC 4214-1. The central object has approximate pixel coordinates (456, 461) and J2000 coordinates $12^{h}15^{m}39^{s}.41$, $36°19'36''.0$.

[c] Flux at 2200 Å in units of 10^{-17} erg cm^{-2} s^{-1} $Å^{-1}$.

while knot 4 may correspond to a faint source in the UV image (§ 3.3). In addition to the bright central object, we visually identified 212 faint sources in this image. Automated identification routines, such as DAOFIND, yield numerous spurious detections of structures related to the point spread function of the bright central object. Despite careful inspection of the image and comparison with a library point spread function, it is still possible that a small fraction of the features we identified as sources are actually structures in the point spread function and that we missed some true sources, in particular some of the fainter ones.

Core aperture photometry was performed on the sources using routines within IRAF. Because of the extended nature of the aberrated point spread function, the observed counts in both an object aperture and the corresponding background annulus have contributions from the background and the source, respectively. In order to account for the source contribution to the counts in the background annulus, as well as to determine the total source flux, it is necessary to determine the fraction of the total source flux enclosed in the various apertures. We obtained from STScI a point spread function appropriate for the F220W filter and the detector configuration and determined the encircled energy fraction, ϵ, as a function of radius from the central peak. A plot of the encircled energy fraction is given in Figure 2. The value of ϵ has been normalized to unity at a radius of 130 pixels ($\sim 3''$). The total flux F_t (counts s^{-1}) for each object and the associated background rate B (counts s^{-1} pixel^{-1}) were derived from the count rates measured in the object aperture F_s and the background annulus F_b with the equations

$$F_t = \frac{F_s A_b - F_b A_s}{\epsilon_s A_b - \epsilon_b A_s}\,, \tag{1}$$

and

$$B = \frac{F_b \epsilon_s - F_s \epsilon_b}{\epsilon_s A_b - \epsilon_b A_s}\,, \tag{2}$$

where A_s is the total area of the object aperture in pixels, A_b is the area of the background annulus in pixels, ϵ_s is the encircled energy fraction within the object aperture, and ϵ_b is the fraction of source energy contained in the background annulus. The derivation of these equations is given in the Appendix. We chose a background annulus with an inner radius of 5 pixels and outer radius of 10 pixels. Results from tests on simulated FOC images indicated that a circular object aperture with a radius of 2.5 pixels provides the best estimate of the true count rates for point sources. Errors on the total count rates were derived by assuming Poisson statistics; however, our simulations indicated that the derived fluxes have an uncertainty of about 20%.

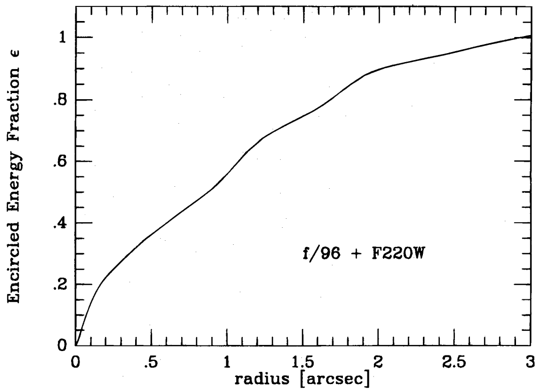

FIG. 2.—Encircled energy fraction ϵ within radius R as a function of R for the f/96 configuration with the F220W filter. The encircled energy is normalized to unity at $r = 3''$.

The total count rates were converted to fluxes by multiplying by the inverse sensitivity, U. Assuming a power-law form for the flux distribution ($F_\lambda \propto \lambda^\beta$), with an index of $\beta = -1.8$ (§ 4.1), and taking into account a format sensitivity factor of 1.25 (Greenfield 1994), we find $U = 7.94 \times 10^{-17}$ erg cm^{-2} s^{-1} Å^{-1} for the particular instrument and filter configuration appropriate for our observations. *HST* instrumental magnitudes were calculated as follows:

$$m_{2200} = -21.10 - 2.5 \log (F_t U)\,. \tag{3}$$

An uncertainty of 20% in F_t corresponds to an uncertainty of about 0.2 mag in m_{2200}. Relative positions, fluxes, and magnitudes of the sources seen in Figure 1 are listed in Table 1.

We attempted to determine the sizes of the individual objects in the FOC image. Experiments on test images indicated that the nominal value of the width of the point spread function (FWHM $\approx$ 3 pixels) could be recovered for point sources by fitting a Gaussian to the observed surface brightness profiles and restricting the fit to the area within 2 pixels of the center of each source. We applied this technique to the objects seen in the FOC image and found that most of these objects are unresolved (FWHM $\leq$4 pixels). A few objects were marginally resolved with FWHM values $\leq$8 pixels (i.e., effective radii $\leq$2 pc).

3.2. *Luminosity of Central Object* (*NGC 4214-1*)

As mentioned above, the count rate from the central object was high enough that this portion of the image suffers from roll-over and substantial nonlinearity. Therefore, the procedure described above could not be used to determine the flux. Instead, we took advantage of the extended wings of the aberrated point spread function to estimate the total flux for this source. We subtracted the fainter sources from the image and then determined the surface brightness profile of the central source. By fitting the wings of the observed surface brightness profile to those of the normalized point spread function, and using $U = 7.94 \times 10^{-17}$ erg cm^{-2} s^{-1} Å^{-1}, we find NGC 4214-1 to have a total flux of 2.46×10^{-14} erg cm^{-2} s^{-1} Å^{-1} or a magnitude $m_{2200} = 12.92$. Again, we estimate the uncertainty on this flux value to be about 20%, or 0.22 mag. This flux estimate assumes that the central object is a point source. Unfortunately, the surface brightness profile does not allow us to distinguish unambiguously between a point source and an extended source, but it is consistent with the assumption of a point source. Furthermore, the region of nonlinearity and roll-over is contained within a diameter of $r \lesssim 10$ pixels; if the central source is extended, it must have a diameter $\lesssim 0\farcs2$ (or $\lesssim 5$ pc). With the color excess derived below (§ 4.1), the extinction law of Kinney et al. (1993), and the assumed distance of 4.1 Mpc, the FOC flux of NGC 4214-1 corresponds to a continuum luminosity at 2200 Å of $L_{2200} = 1.32 \times 10^{38}$ ergs s^{-1} Å^{-1}. This intense but small (diameter $\lesssim$5 pc) starburst knot has properties (e.g., size, 2200 Å luminosity) very similar to those of the knots found in the central starburst region of the blue compact dwarf

1996ApJ...465..717L

galaxy He 2–10 observed by Conti & Vacca (1994) using an identical FOC setup. The 2200 Å luminosity of NGC 4214-1 is also similar to the starburst knots in the galaxies observed by Meurer et al. (1995) with the FOC.

NGC 4214-1 contributes only a negligible fraction to the total optical luminosity of NGC 4214. Using $M_{2200} = -15.9$ (Table 1) and the relations of Leitherer & Heckman (1995, hereafter LH) we find $M_B \approx -13$ for NGC 4214-1. This can be compared with the total blue magnitude of NGC 4214: $M_B = -18.8$ (SF91). Similarly, all other individual sources detected in the FOC image are negligible (see below).

3.3. *Luminosity Function of Other Sources*

In Figure 3 below we present the 2200 Å luminosity function of the fainter sources seen in the FOC image. The central object NGC 4214-1 is well separated from the others at the bright end of the distribution and is not included in the figure. This luminosity function has been constructed using a distance modulus of 28.06 mag ($D = 4.1$ Mpc), and assuming the color excess derived for NGC 4214-1 [$E(B-V) = 0.09$ mag; see § 4.1] applies to the entire FOC field. For the extinction curve given by Kinney et al. (1994), this color excess corresponds to an extinction at 2200 Å of $A_{2200} = 0.72$ mag. The completeness limit is estimated to be approximately $m_{2200} = 19.5$ mag, or $M_{2200} = -9.3$ mag, although it certainly varies substantially across the image because of the variable background level produced by the scattered light from the central source.

We suggest that most of the fainter sources are luminous hot stars. In Figure 4 we show the temporal evolution of M_{2200} for a 100 $M_\odot$ star from the zero-age main sequence up to the post–Wolf-Rayet phase. The values were calculated using the method of LH. The most massive stars are predicted to have $M_{2200} \approx -10$, which is brighter than many of the fainter sources detected. As an additional test, we have compared the observed luminosity function with that inferred for the stars in the 30 Dor region. We used a sample of stars from the work of Parker (1992, 1993) and approximated the $M_{2200} - M_V$ color as -3 mag (accurate to about ±0.3 mag for late O- and early B-type stars, as determined from the Bruzual spectral atlas in the synphot package in IRAF). The sample drawn from Parker's study includes only the brightest and bluest stars, or stars with known O, B, or W-R spectral classifications, located in a $\sim 7' \times 7'$ (or 105×105 pc^2) region centered on R136, the central ionizing cluster in 30 Dor. We wanted a sample to consist entirely of hot stars; appreciably cooler stars, such as G and later type supergiants, have negligible radiation at 2200 Å, and their exclusion will not affect the luminosity function derived. We see that the point sources in NGC 4214 have a luminosity function very similar to the brighter stars in 30 Dor. More importantly, the luminosity function of the sources in NGC 4214 spans the same magnitude range as that for the stars in 30 Dor. Of course, the apparent magnitude limit in NGC 4214 is brighter than that of 30 Dor, so the number counts turn over at a brighter magnitude. Parker's (1992, 1993) ground-based images suffer from crowding due to the limited spatial resolution, and therefore some of the brightest objects in his sample are not individual stars but actually small clusters of stars. This may also be the case for NGC 4214, where the brightest sources in our image (outside of the central knot) may actually be small clusters of hot stars. Under the assumption that *all* of the objects are individual stars, we have fitted the luminosity function presented in Figure 4 with a power law over the magnitude range -12.5 to -9 in M_{2200}. We find that the number of objects N within the luminosity bin L to $L + dL$ varies as $L^{-0.9}$. The power-law index is very close to a luminosity function in the B band found by Malumuth & Heap (1994) for stars located between 4″ and 35″ from R136a in 30 Dor ($L^{-0.83}$).

Our 22″ × 22″ FOC image of NGC 4214 covers approximately 440 × 440 pc^2, substantially larger than the 30 Dor region studied by Parker (1992, 1993). Although the number of hot stars surrounding NGC 4214-1 is about 30% larger than in 30 Dor, the stellar surface density is about a factor of 20 smaller. Thus, the immediate surroundings of NGC 4214-1 have relatively *fewer* hot stars than the 30 Dor region surrounding R136. We will show, however, that the *starburst knot* itself is *brighter* than the central 1′ × 1′ region of 30 Dor (§ 6). The density contrast of NGC 4214-1 between the core and the immediate surroundings is similar to that of the Galactic cluster NGC 3603. Moffat, Drissen, & Shara (1994) found from *HST PC* imaging that NGC 3606 has a central star density very similar to that of R136. However, NGC 3603, like NGC 4214-1, has a very low star density outside the central core.

Knot 4 in SF91's notation may correspond to source 127 in Table 1; the separation from knot 1 is roughly correct. Although it is one of the brighter objects, it is still about 4.5 mag *fainter* than NGC 4214-1 at 2200Å. The latter object certainly dominates the ionization of the interstellar gas. It

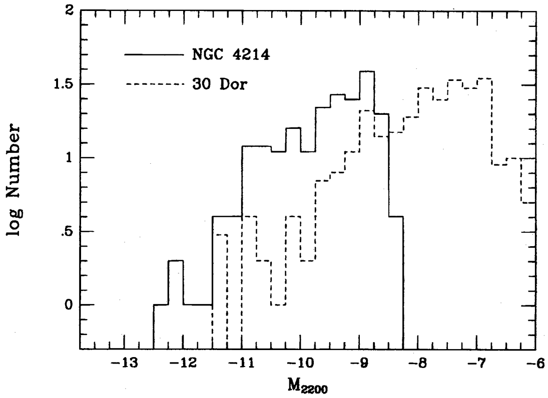

FIG. 3.—Number of objects in 0.25 magnitude bins detected in the FOC image of NGC 4214.

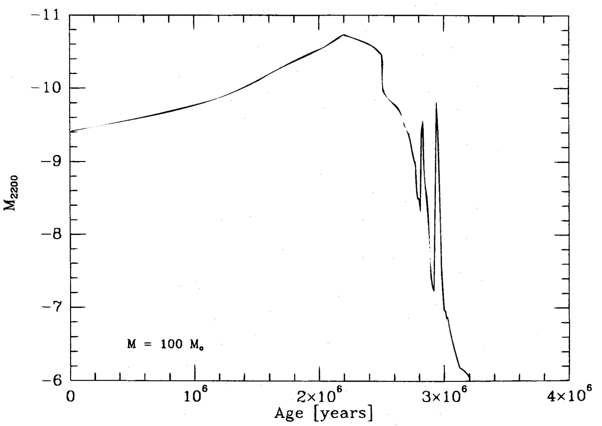

FIG. 4.—Theoretical M_{2200} of a star having an initial mass of 100 $M_\odot$ based on LH's models.

is possible that the continuum of knot 4 detected by SF91 is scattered light from knot 1. Curiously, the Hα emission in this region seems to be more closely centered on knot 4, rather than knot 1 according to Figure 3 of SF91, but the optical line measurement we will use (§ 5.1) includes both regions.

4. SPECTRAL PROPERTIES OF NGC 4214-1

4.1. *Observed Ultraviolet Spectrum*

In Figure 5 we show the UV spectrum of NGC 4214-1 obtained with the FOS. The final spectrum is in the rest frame of NGC 4214-1, which has an observed velocity of approximately +300 km s^{-1} (de Vaucouleurs et al. 1991), and was generated by merging the two spectra obtained with gratings G130H and G190H. Comparison of the flux levels in the overlapping region near 1600 Å suggests no significant (<10%) offset. The slope of the continuum between 1200 and 1900 Å, defined by $F_\lambda \propto \lambda^\beta$, is $\beta = -1.8$. This slope agrees very well with the value derived by Kinney et al. (1993), who found $\beta = -1.85$ from *IUE* observations of the galaxy.

The observed FOS flux at 2200 Å (approximately the effective wavelength of the FOC image) is found to be 1.6×10^{-14} erg cm^{-2} s^{-1} $Å^{-1}$, about 65% of the value we derived above from the FOC image (§ 3.2). This difference is a little larger than we would have anticipated given our formal uncertainties. The *IUE* flux measured by Huchra et al. (1983) is about a factor of 3 larger than our FOS value. The *IUE* observations refer to an area of 10″ × 20″, which includes the region in the FOS aperture. Our FOC image reveals that the central starburst knot NGC 4214-1 is by far the brightest individual source at 2200 Å (see Table 1). However, all other sources combined in the FOC field of view contribute approximately the same flux as NGC 4214-1 itself. If the *IUE* slit was set on NGC 4214-1, as indicated by Fig. 4 of Huchra et al., it will contain many of the sources within our FOC image. We are unable to reconstruct which sources actually fell within the *IUE* slit position of Huchra et al., but a rough estimate suggests that the *IUE* and FOC fluxes agree to within a factor of 2. Therefore, possible uncertainties in flux values of a factor of 2 will need to be kept in mind in what follows.

Young starburst regions have rather similar UV energy distributions for a wide range of metallicities, initial mass functions, and ages. LH calculated a model grid, which predicts $\beta = -2.6 \pm 0.3$ for metallicities Z in the range $0.1\ Z_\odot < Z < 2\ Z_\odot$, IMF slopes α between 2.35 and 3.3, upper cutoff masses $M_{\rm upp}$ between 30 and 100 $M_\odot$, and ages $t < 10$ Myr. NGC 4214-1 is within this parameter range, as we show below (§ 4.2). The redder observed continuum of NGC 4214-1 ($\beta = -1.8$) can thus be attributed to dust extinction within the galaxy. (Galactic foreground extinction is negligible at the latitude of NGC 4214.) Using the mean extragalactic extinction law derived by Kinney et al. (1994) from a sample of galaxies observed with *IUE*, we find a relation between the color excess and the change in continuum slope produced by reddening,

$$E(B-V) = 0.11\delta\beta\ , \qquad (4)$$

where $\delta\beta$ is the increase of the continuum slope of a stellar spectrum between 1200 and 1900 Å because of selective dust extinction. The coefficient of 0.11 applies to a wavelength of 1550 Å but the relation is a reasonably good approximation for the mean slope between 1200 and 1900 Å. Equation (4), then, suggests $E(B-V) = 0.09$ mag. We use this value and the reddening law of Kinney et al. (1994) to deredden the continuum of NGC 4214-1 at optical and UV wavelengths.

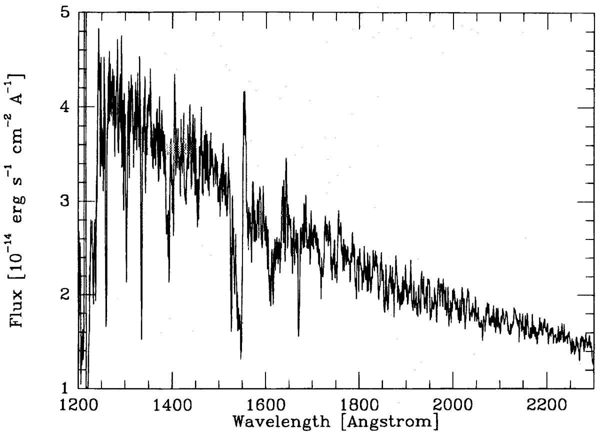

FIG. 5.—Ultraviolet spectrum of NGC 4214-1 observed with the FOS through a 1″ aperture.

The UV spectrum, between 1200 and 1800 Å, of NGC 4214-1 exhibits numerous stellar and interstellar lines (see Fig. 5). Equivalent widths of all lines are given in Table 2. Column (1) of this table lists the line identification, the approximate *laboratory* wavelengths are in column (2), and the equivalent widths W_λ are in column (3) (positive values for absorption, negative for emission). Crosses in columns (4) and (5) indicate whether the line is of stellar or interstellar origin in NGC 4214-1.

The spectral lines seen in the FOS spectrum (Fig. 5) are morphologically similar to those in the *IUE* spectrum shown by Huchra et al. (1983) with the exception that the broad emission feature seen in their Figures 1 and 3 at ~1480 Å is *not* seen in the *HST* spectrum. While this feature has been attributed to N IV] λ1483 in some *IUE* spectra of hot stars and starburst galaxies, it is most likely a camera artifact (Crenshaw, Bruegman, & Norman 1990). Of course, the FOS spectrum of NGC 4214 has much better signal-to-noise (S/N) and spectral resolution than the *IUE* spectrum; the interstellar lines are clearly narrower than the stellar features.

The strongest *stellar* lines are C IV λ1550, Si IV λ1400, and N V λ1240. Narrow absorption components of these resonance transitions are located at essentially the laboratory

TABLE 2

MEASURED EQUIVALENT WIDTHS

Line (1)	λ (Å) (2)	W_λ (Å) (3)	Stellar (4)	Interstellar (5)
N V	1241	...	×	×
Si II	1260	2.0		×
O I + Si II	1303	1.6		×
C II	1335	1.8		×
Si IV abs	1398	3.9	×	×
Si IV emi	1398	−0.3	×	
C III	1428	0.7	×	
Si II	1526	1.5		×
C IV abs	1550	5.9	×	×
C IV emi	1550	−1.8	×	
Fe II, Fe III......	1610	2.8	×	×
He II	1640	−0.3	×	
Al II	1671	1.9		×
N IV	1719	1.5	×	

1996ApJ...465..717L

wavelengths (in the rest frame of NGC 4214) and are due to absorption within the interstellar medium of NGC 4214 itself. The C IV, Si IV, and N V doublets are clearly resolved, but N V is severely blended with interstellar Lyman-α. We note that the continuum flux is less certain around the N V line because of the strength of Lyman-α, which precludes any reliable measurement of the equivalent width of N V $\lambda1240$.

A comprehensive discussion of the UV line spectrum of a young starburst region can be found in Leitherer, Robert, & Heckman (1995, hereafter LRH). Based on their results it is clear that the UV spectrum of NGC 4214-1 is dominated by a very young, massive stellar population. Only a few objects in the atlas of star-forming galaxies published by Kinney et al. (1993), for example, show P Cyg profiles of C IV $\lambda1550$ and Si IV $\lambda1400$, which are indicators of the youngest, most massive stars. Similarly, NGC 4214 is among the bluest objects in the sample of Kinney et al., a result that implies a very young starburst with little reddening due to dust.

4.2. *Evolutionary Synthesis Models*

We modeled the UV spectrum of NGC 4214-1 with the evolutionary synthesis technique described by LRH. The reader is referred to that paper for details concerning the modeling techniques and the models themselves. Examples of applications of the models to data can be found in Robert, Leitherer, & Heckman (1993) and Vacca et al. (1995). Briefly, a stellar spectral library constructed from *IUE* high-dispersion spectra of O and W-R stars and from low-dispersion spectra of B stars is coupled with an evolutionary synthesis code to compute a synthetic spectrum from 1200 to 1800 Å for a set of input parameters. These parameters are the star formation history, which can be either one of the two limiting cases of continuous star formation or an instantaneous burst; the age t of the starburst, which is defined as the time elapsed since the onset of the continuous star formation or since the occurrence of the burst; the IMF, parameterized as a power law with exponent α between the upper and lower mass limits $M_{\rm upp}$ and $M_{\rm low}$; and the metallicity Z of the stars and gas. We note that the theoretical spectra include the contribution from nebular continuous emission. Nebular emission lines are not included.

Metallicity is treated self-consistently in this code with respect to the stellar atmospheres and the evolutionary models, but not for the spectral library. The stars in the spectral library have the chemical composition of stars within about 2.5 kpc of the Sun (i.e., solar or somewhat lower). The metallicity of NGC 4214 is 0.5 $Z_\odot$ (Huchra et al. 1983), which would require stars with slightly lower metallicity than in our library. Ultraviolet spectra of a significant number of hot, metal-poor stars having a spectral resolution and S/N adequate for our purpose do not yet exist. We will return to this point below when we assess the uncertainties of our models. We performed test calculations to study the influence of metallicity on the evolutionary tracks and the atmospheres. Except for the predicted number of W-R stars, the models are not very sensitive to Z in the range $0.25\ Z_\odot \leq Z \leq Z_\odot$. Therefore, we calculated all models under the assumption of solar composition.

As discussed by LRH, the five principal UV lines constraining the stellar content are N V $\lambda1240$, Si IV $\lambda1400$, C IV $\lambda1550$, He II $\lambda1640$, and N IV $\lambda1720$, all of which are present in NGC 4214-1. However, N V $\lambda1240$, He II $\lambda1640$, and N IV $\lambda1720$ are too weak to be useful as primary indicators, given the noise level. Therefore, our approach is to use Si IV $\lambda1400$ and C IV $\lambda1550$ as our principal line features; we then compare the observed and theoretical profiles of N V $\lambda1240$, He II $\lambda1640$, and N IV $\lambda1720$ to check for consistency.

Both burst and continuous formation models provide good fits to the observed spectrum. The profiles of C IV $\lambda1550$ and Si IV $\lambda1400$ agree quite well with the observations, although the observed C IV emission is slightly stronger than in the models. We could not otherwise find a model that would match the emission component and at the same time not have significantly too strong an absorption. Nebular C IV probably does not contribute significantly to the observed emission, as there is no indication of nebular C III] $\lambda1908$, which should be present if nebular C IV $\lambda1550$ is strong. Moreover, C IV $\lambda1550$ is broad, as expected if it is produced in stellar winds. A contribution from WC stars is possible (§ 5.2). Another discrepant line is N V $\lambda1240$, whose strength is overestimated by the models. However, as we emphasized before, this line is situated in the Lyman-α wing, and the true continuum is uncertain.

The predicted strengths of He II $\lambda1640$ and N IV $\lambda1720$ agree with the observations; the former line is produced by W-R stars of type WN. The presence of W-R stars *independently* implies an age of a few Myr for the starburst, although we have inferred an age of 4–5 Myr from the best fit to the C IV $\lambda1550$ and Si IV $\lambda1400$ line profiles.

The two theoretical models for the burst and constant star formation that fit the *line spectrum* best are shown, along with the monochromatic luminosity L_λ from 1200 to 1800 Å, dereddened with the extragalactic extinction law of Kinney et al. (1994), in Figure 6. The theoretical spectra were calculated with $t = 5$ Myr, $M_{\rm upp} = 80\ M_\odot$, $\alpha = 2.35$ (continuous star formation) and $t = 4$ Myr, $M_{\rm upp} = 80\ M_\odot$, $\alpha = 3.00$ (burst). We will use these continuum fitting models to predict the number of ionizing stars (§ 5.1).

Formally, the continuous formation model gives a slightly better fit to the line profiles than the burst model. However, in view of systematic uncertainties, such as the metal abundance or the contribution of interstellar lines, we do not claim to be able to distinguish between the two cases from these data. The physical size of NGC 4214-1 (diameter

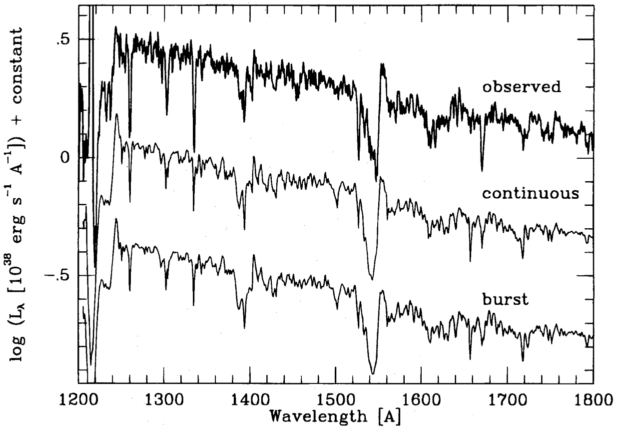

FIG. 6.—Comparison between the dereddened monochromatic luminosity (*top*) and the best-fit models for continuous star formation (*middle*) and an instantaneous burst of star formation (*bottom*). Parameters for the theoretical spectra are $t = 5$ Myr, $M_{\rm upp} = 80\ M_\odot$, $\alpha = 2.35$ (continuous) and $t = 4$ Myr, $M_{\rm upp} = 80\ M_\odot$, $\alpha = 3.00$ (burst). For clarity, the theoretical spectra have been shifted vertically by -0.47 (continuous star formation) and -0.89 (burst).

$\lesssim 5$ pc, corresponding to crossing times well below 1 Myr; § 3.2) suggests the burst model is more appropriate. In any case, the agreement between the theoretical and observed spectra bolsters our confidence in the evolutionary synthesis models. We can draw the following conclusions. (1) We observe a hot star population containing massive stars with initial masses of up to 60–80 $M_\odot$. (2) The starburst is evolved. The presence of at least some O supergiants is required, i.e., $t \approx 4$–5 Myr. (3) If the IMF follows a power law, its exponent is between 2.35 and 3.00.

These ranges of $M_{\rm upp}$, t, and α are conservative estimates derived from line-profile fitting, taking into account uncertainties due to the blending with interstellar lines, continuum fitting, and metallicity effects. We do not show theoretical spectra for other model parameters. They can be found in LRH and the sensitivity to IMF and age can be assessed.

Earlier we noted the inconsistency between the metallicity of the library stars ($Z \approx Z_\odot$) and that of NGC 4214 ($Z = 0.5\ Z_\odot$). Observations of individual hot stars in the Magellanic Clouds suggest that O stars in a low-metallicity environment have weaker spectral lines and lower wind velocities than their Galactic counterparts (Walborn et al. 1995). The LMC has $Z = 0.3\ Z_\odot$ (Dufour 1984; Mathis, Chu, & Peterson 1985; Rosa & Mathis 1987) so that the properties of its stellar population will give an upper limit for the correction to be applied to our results if Z is taken into account. Walborn et al. showed that metallicity effects in the LMC are rather modest, as the line strengths of the strongest stellar-wind lines are comparable to those of Galactic stars. Wind velocities are comparable in the LMC and in the Galaxy. In contrast, stars in the Small Magellanic Cloud, which has even lower metallicity, do have weaker lines and lower wind velocities (see the study of Puls et al. 1996). This suggests that significant metallicity effects set in at $Z \leq 0.3\ Z_\odot$ and our modeling of NGC 4214-1 at $Z = 0.5\ Z_\odot$ with a stellar library at $Z_\odot$ is probably valid.

4.3. *Interstellar Lines*

The strongest interstellar lines in NGC 4214 (which are not also produced in O-star winds) are due to Si II λ1260, O I/Si II λ1300, C II λ1335, Si II λ1526, and Al II λ1670. These lines are broader than expected from the nominal FOS resolution for a point source. We attribute this to the combined effects of NGC 4214-1 not being a point source and macroscopic velocities in the interstellar medium. We measured no significant wavelength shift with respect to the rest frame of NGC 4214. This suggests that the interstellar material has no detectable velocity component relative to the stellar component resulting from a large-scale galactic superwind, (e.g., Marlowe et al. 1995). Lines such as Si II λ1260, C II λ1335, or Al II λ1670 could in principle also have a stellar origin in mid- to late-B stars (see Rountree & Sonneborn 1993), but such stellar lines are much broader than the interstellar counterparts.

From our analysis of the UV continuum we found that NGC 4214-1 has very little internal reddening by dust. However, the interstellar lines are systematically stronger than those in the spectra of our library stars, most of which have *higher* extinction. The immediate conclusion is that the interstellar medium in NGC 4214-1 is different from that in the solar neighborhood. We can exclude different ionization states as an explanation for the different line strengths, as both low ionization states (e.g., C II λ1335) and high ionization states (e.g., the interstellar contribution to C IV λ1550) are stronger in NGC 4214-1. The stronger interstellar lines in NGC 4214-1 might be the result of a higher gas density (i.e., a larger gas to dust ratio), as might be expected in star-forming regions.

However, the different strengths of the interstellar lines in the observed and the synthesized spectra are more likely a result of different velocity dispersions sampled by the sight lines toward NGC 4214-1 and the individual stars in the spectral library. All strong interstellar lines in Table 2 are either saturated or close to the horizontal part of the curve of growth even in relatively unreddened library stars. Higher $E(B-V)$ (e.g., because of a larger distance) will not increase the equivalent widths substantially unless the line of sight crosses individual gas clouds having significantly different velocities. This is in contrast with the situation in giant H II regions (and NGC 4214-1), which have highly supersonic turbulent velocities (Muñoz-Tuñon 1994). The resulting higher velocity dispersion gives rise to either broader interstellar absorption lines or, more likely, to many individual, strong interstellar absorption components. The sum of the equivalent widths of all components will be larger than the equivalent width of an individual strong line in the absence of turbulence. Observed velocity dispersions in giant H II regions are between 10 and 30 km s^{-1} (Muñoz-Tuñon 1994). This is well below the resolution limit of the FOS, which will record the individual components as one blend with a correspondingly higher equivalent width.

The interstellar absorption components of the Si IV doublet at 1394 and 1403 Å seem to have an additional satellite line blueshifted by about 2 Å. The strengths of these blue features are only slightly above the noise level, and their reality may be doubtful. Their wavelengths coincide with the wavelengths expected for a Galactic foreground absorption of Si IV. An additional component consistent with this interpretation may also be present in C IV λ1550. On the other hand, there is no clear indication for such a feature in most other interstellar lines.

5. COMPARISON WITH GROUND-BASED DATA

5.1. *The Number of O Stars and the Ionizing Photon Fluxes*

Comparison of the *HST* data with existing ground-based observations requires considerable caution because of the insufficient spatial resolution of such data. Furthermore, these analyses utilize properties of the *ionized gas* to infer hot star statistics, whereas UV spectra sample the hot stars directly. The ionized gas and the hot stars may not be completely cospatial, and the *local* interstellar medium might be density, rather than ionization, bounded (i.e., Lyman continuum photons could be escaping the region).

The most extensive studies of NGC 4214 are those by Hunter (1982), Huchra et al. (1983), and SF91. Hunter (1982) presented optical echelle spectra and Hα video images of star-forming regions in 15 irregular galaxies, including NGC 4214. The position of knot 4 roughly coincides with the central position of region 6 in Hunter's notation, but region 1 is also within its boundaries. Hunter's Table 3 contains her echelle data, and her Table 7 gives the details of the video images. Huchra et al. (1983) studied NGC 4214 in the infrared, optical, and ultraviolet, giving the Hβ flux in their Table 2. SF91 obtained long-slit optical spectra covering several star-forming regions of NGC 4214.

Detailed examination of the measured emission line fluxes in the various papers indicates a serious lack of consistency in the values, probably because different apertures were used and different emission areas were being sampled. The ionized gas in the vicinity of NGC 4214-1 is not cospatial with the continuum emission (see SF91, Fig. 3; § 3.3). At our request, Deidre Hunter recently reobserved her region 6 with a CCD imager and a narrow-band filter centered on Hα. Her image is reproduced in Figure 7. The maximum of Hα emission is not centered on NGC 4214-1. There is very low Hα emission at the location of NGC 4214-1, which is at the edge of an Hα hole. The stellar cluster of NGC 4214-1 itself is not visible on this image. The continuum-subtracted image yields an Hα flux of 3.6×10^{-13} erg cm^{-2} s^{-1} for a roughly 5″ diameter region. This value is intermediate between the published data referred to above. This Hα flux includes the regions of both NGC 4214-1 and knot 4 of SF91.

The new Hα flux was corrected for reddening using the extinction law given by Kinney et al. (1994) with $E(B-V) = 0.09$ mag, inferred from the observed UV continuum (§ 4.1). This value agrees with the extinction derived from the Balmer decrement by SF91. The resulting dereddened flux was combined with a distance of 4.1 Mpc to determine the Hα luminosity and the number of Lyman continuum photons $N_{\rm Lyc}$ emitted by the hot star population within the starburst knot. We assumed that $T_e = 8800$ K and $n_e = 100$ cm^{-3}, as given in Hunter (1982). We find $N_{\rm Lyc} \approx 5 \times 10^{50}$ s^{-1}. The two best-fitting evolutionary synthesis models shown in Figure 6 predict $N_{\rm Lyc} \approx 1.9 \times 10^{51}$ s^{-1} (for a burst) and $N_{\rm Lyc} \approx 4.1 \times 10^{51}$ s^{-1} (for continuous star formation). The model values of $N_{\rm Lyc}$ are 4–8 times larger than that inferred from the newly determined ground-based Hα line measurement. The 5″ diameter clearly encompasses NGC 4214-1; this Hα emitting gas covers a much larger volume than the stellar starburst itself.

We note that the Hβ emission-line equivalent width of NGC 4214-1 measured by SF91 (W_λ(Hβ) = 14 Å) is a factor of a few smaller than in our models, which predict a value around 50 Å (see LH). W_λ(Hβ) is one of the most robust model predictions; Stasińska & Leitherer (1996) found very good agreement between observed and predicted Hβ equivalent widths in a sample of 100 metal-poor H II galaxies. Although it is possible that such agreement no longer holds for metal-rich ($Z \geq Z_\odot$) galaxies (García-Vargas & Díaz 1994) if contamination by an underlying older stellar population plays a significant role, this cannot fully explain the discrepancy seen in NGC 4214 ($Z = 0.5\ Z_\odot$). The low

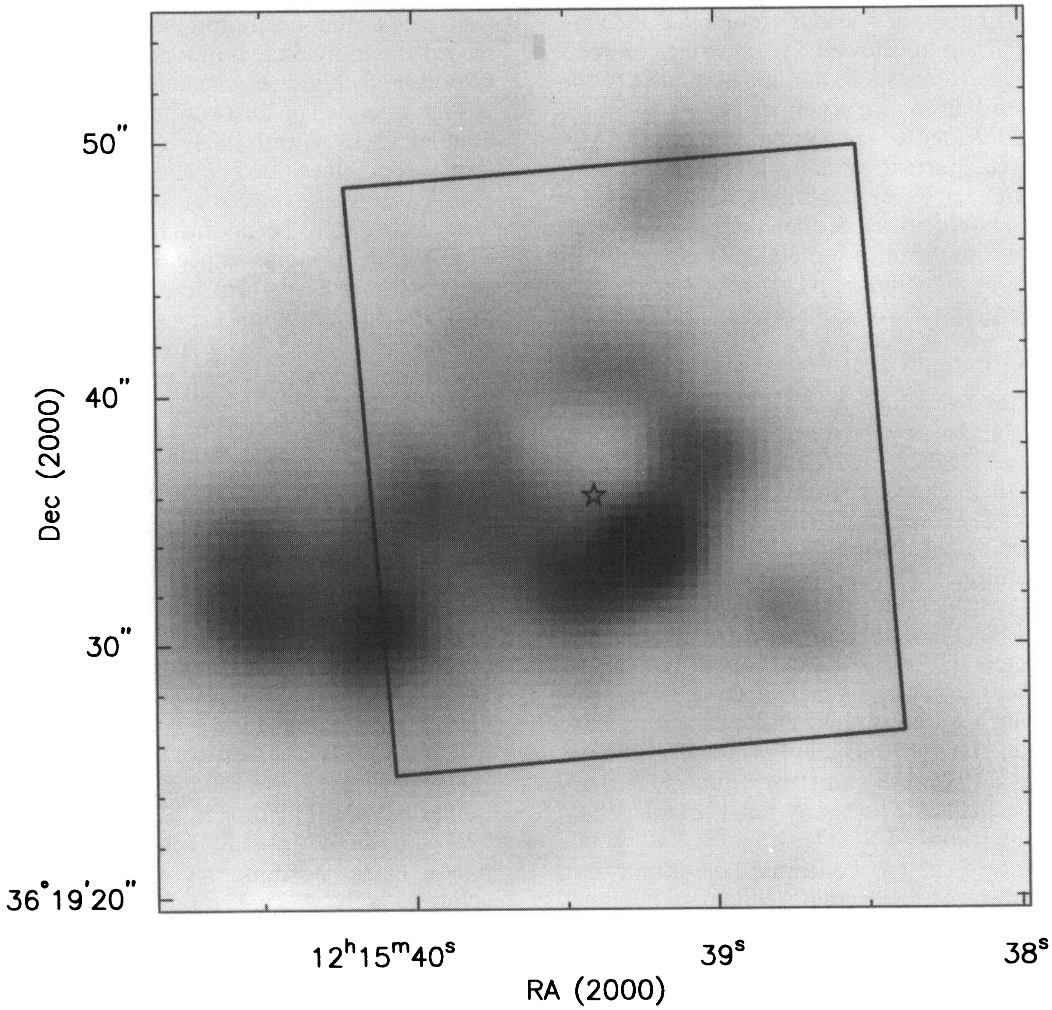

FIG. 7.—Continuum subtracted Hα image of NGC 4214 obtained by D. Hunter at the Lowell Observatory 1.8 m telescope on 1995 April 29. North is up and east to the left. The box has a size of 22″ × 22″ and outlines the region observed with the FOC. The star denotes the position of NGC 4214-1. Note that NGC 4214-1 is not located at an emission peak in the Hα image, but rather lies at the southern edge of a circular "hole" in the Hα emission. None of the objects detected in the FOC image are coincident with the peak of the Hα emission seen in the image (to the SW of NGC 4214-1).

values of Hα line flux and $W_\lambda(\mathrm{H}\beta)$ in NGC 4214-1 suggest to us that a significant fraction of the Lyman continuum photons might be escaping from the H II region, which would then be *density bounded*.

It would thus appear that the ground-based *nebular recombination* values of N_{Lyc} cannot be used to reliably infer the O star population in the case of NGC 4214-1. Hydrogen recombination line fluxes are the most common indicator of hot stars in galaxies, but they provide a reliable estimate of the hot star content (see Vacca et al. 1995) only if the nebular region is completely ionization bounded. In the case of NGC 4214-1, however, we infer from the UV luminosity in the FOS spectrum that many more OB stars are present than are accounted for by nebular recombination lines. SF91 considered this possibility, but were unable to test it with their ground-based data. We cannot exclude an alternative situation where the gas we observe is virtually unextinguished, while the rest of the gas is so extinguished that it cannot be observed at all. This seems unlikely, especially since the stars are not extinguished, but it could result from a dense, dusty molecular torus around the stars.

Using the *model parameters* we adopted above, we find the ionizing flux is produced by about 380 O stars of all luminosity classes for the two cases of a burst and continuous star formation. (The fact that the O star numbers agree is coincidental. In general, burst and continuous star formation models with the same IMF and age predict different O star numbers after normalization to the same ultraviolet luminosity, especially during epochs when the most massive stars have exploded as supernovae.)

The total mass of stars with masses above 1 $M_\odot$ formed in the star-formation episode is on the order of 10^5–10^6 $M_\odot$. The exact value is strongly dependent on the IMF below 10 $M_\odot$, which is unconstrained in our study.

CO (2–1) and (1–0) observations of the region around NGC 4214-1 were obtained by Becker et al. (1995). A CO complex having a gas mass of 10^7 $M_\odot$ was detected and resolved into three components. The ringlike structure of faint Hα emission is located at the interface between the two more prominent CO components. The eastern component has a broader CO profile (FWHM = 23 km s^{-1} versus 15 km s^{-1} in the western part) and overlaps with the optical location of NGC 4214-1. Stellar winds from the recent starburst may be responsible for the kinematics measured in the CO line.

5.2. *The Number of W-R Stars*

We were initially motivated in our study of NGC 4214-1 by the detection of a broad emission feature from Wolf-Rayet stars in the spectrum obtained by SF91. Based on the strength of the 4660 Å blend, they inferred that 144 W-R stars were present and estimated the ratio of the numbers of W-R to O stars to be approximately unity. We have reexamined the number of W-R stars using the more advanced analysis presented by Vacca & Conti (1992). These authors showed that the properties of the W-R emission blend at 4660 Å can differ from galaxy to galaxy because of contributions from other emission lines, both nebular and stellar. The most important stellar emission feature other than He II λ4686 is N III λλ4634, 4640 from W-R stars of WNL type (Vacca & Conti 1992). A nebular [Fe III] λ4658 line is also sometimes present in the 4660 Å blend. From the wavelength morphology of the broad emission in NGC 4214-1, both of these blending lines are present in the optical spectra of SF91. Some contribution of λ4650 C III from WC stars may also be present. We initially estimate that about half of the flux in the 4660 Å blend detected by SF91 is caused by He II λ4686. The inferred luminosity of He II is then $L(\lambda4686) = 4.2 \times 10^{37}$ ergs s^{-1}, for our adopted distance of 4.1 Mpc. The average luminosity of the He II λ4686 line in single WNL stars is $L(\lambda4686) = 1.7 \times 10^{36}$ ergs s^{-1}, with a variation of about a factor of 3 around the mean (Vacca 1992; Vacca & Conti 1992). This yields a total of 25 WNL stars in NGC 4214-1, much smaller than that originally estimated by SF91, who assumed a distance to NGC 4214 of 5.4 Mpc and used the strength of the entire blend to estimate the number of W-R stars.

Based on the detection of C IV λ5808, SF91 propose that NGC 4214-1 also contains WC stars. Mas-Hesse & Kunth (1991) independently report the presence of WC stars in NGC 4214. From a yellow-red spectrum of NGC 4214-1 obtained by W. L. W. S., we have estimated a flux of $\sim 2.5 \times 10^{-14}$ erg cm^{-2} s^{-1} in the C IV λ5808 line. Using the calibration derived by Vacca (1992; see also Vacca & Conti 1992), $L(\lambda5808) = 2.5 \times 10^{36}$ ergs s^{-1} for a single WCE star, we find that this corresponds to approximately 20 WC stars. WN stars have C IV λ5808 line strengths that are typically an order of magnitude lower than in WC stars (Conti & Massey 1989) and do not contribute significantly to the C IV feature in NGC 4214-1.

How would these WC stars affect the λ4660 emission feature? For WC stars in general, the luminosity in the λ4650 C III line is at least as large as that in C IV λ5808 (Brownsberger 1995). For NGC 4214-1, this implies a contribution to the luminosity in the λ4660 blend of 5.1×10^{37} ergs s^{-1}, a little more than *half* the measured strength inferred from SF91. But we have already estimated above that half the blend is contributed by λ4686 He II, and at least part of the rest by N III and [Fe III]. We clearly cannot simultaneously account for *both* the WNL and WC type contributions to the λ4660 emission blend, although it is also clear that both kinds of stars are present in roughly equal numbers. Keeping in mind uncertainties of a factor of 2, we give a *best guess* estimate that approximately 15 WN and 15 WC stars are present in NGC 4214-1.

Our evolutionary synthesis *models* predict 43 and 18 W-R stars for the burst and continuous star formation scenarios, respectively. The numbers are *very* sensitive to the adopted metallicity, as can be seen from the starburst models (LH). Models with $Z_\odot$ and 0.25 $Z_\odot$ differ by as much as a factor of 4 in their W-R/O ratio, with lower Z resulting in smaller W-R/O. Therefore, our predicted numbers, which are based on $Z_\odot$, might be too high for NGC 4214-1 ($Z = 0.5\ Z_\odot$). Furthermore, evolutionary models for W-R stars are still somewhat uncertain (Maeder & Conti 1994), and the absolute numbers predicted by synthesis models should be viewed with caution. Given these uncertainties, the predicted number of W-R stars in the burst case and that estimated from the ground-based observations are in very good agreement. Note that in this case, as opposed to the *nebular* emission line data, the measured He II λ4686 line corresponds to those stars within the slit and starburst, whereas the *ionized gas* is certainly more extended and may even be density bounded (§ 5.1).

Adopting the number of W-R stars (30) inferred from the broad emission lines and O stars (380) predicted by the burst model leads to a logarithmic ratio for the number of W-R to O stars of approximately −1.1. This value is close to that typically observed for a starburst galaxy having about half solar metallicity (Maeder & Conti 1994; their Fig. 3). The burst model is also consistent with the small physical size of the knot.

6. NGC 4214-1, 30 DORADUS, AND M31 OB 78

30 Doradus in the LMC and its central star cluster R136 is the prototype and the closest example of a giant H II region. Vacca et al. (1995) performed a detailed analysis of its stellar content in the inner 1′ × 1′ and 3′ × 3′, as derived from UV spectra obtained with *IUE*. At a distance of ∼50 kpc these regions have linear sizes of 15 and 45 pc, respectively. For NGC 4214, the region encircled by the FOS aperture has a diameter of ∼17 pc, similar to the smaller of these 30 Dor regions analyzed with *IUE*. This allows a direct comparison of both sets of observations.

The relevant properties of the inner part of 30 Dor found by Vacca et al. (1995) are $N_{\rm Lyc} \approx 1.3 \times 10^{51}$ s^{-1} (inferred from the counts of hot stars); continuum luminosity at 1500 Å of $L_{1500} = 6 \times 10^{37}$ ergs s^{-1} Å^{-1}; Salpeter IMF with $M_{\rm upp} > 50\ M_\odot$; and starburst age $t \sim 3$ Myr. For comparison, we infer essentially the same IMF for NGC 4214-1, but an older age of 4–5 Myr. These quantities are independent of the nebular emission-line diagnostics as they were derived from the UV line spectrum. The (predicted) ionizing fluxes for NGC 4214-1 are 1.9×10^{51} s^{-1} and 4.1×10^{51} s^{-1}, for the burst and continuous star formations models, respectively. We find the continuum luminosity at 1500 Å is 1.67×10^{38} ergs s^{-1} Å^{-1} from our FOS spectrum.

Thus, the predicted number of Lyman continuum photons and the observed UV fluxes both suggest that NGC 4214-1 is roughly twice as luminous as the 1′ × 1′ region of 30 Doradus. We noted above that $N_{\rm Lyc}$ derived for NGC 4214-1 from nebular gas recombination line measurements does not agree with that predicted by our models, and we ascribed the discrepancy to the fact that the starburst region is deficient in ionized gas. Vacca et al. (1995) pointed out that the Kennicutt & Hodge (1986) Hα measurements *inside* the 1′ × 1′ region of 30 Dor imply $N_{\rm Lyc} \approx 1.8 \times 10^{50}$ s^{-1}, a factor of 7 smaller than that inferred from the counts of hot stars. In this case, there is considerable ionized gas well outside the region of the hot stars (they are not cospatial), and this geometry is probably a major reason for the discrepancy for 30 Dor; Vacca et al. (1995) also suggest that *some* fraction the Lyman continuum photons may be leaking out of 30 Dor. Optical direct imaging and long-slit spectroscopy of 30 Dor demonstrate the existence of large numbers of filaments with velocities up to 200 km s^{-1} (Kennicutt & Hodge 1986; Chu & Kennicutt 1994), probably resulting from *previous* star formation activity. Similar structures have been observed in a variety of massive star formation sites (see examples in Tenorio-Tagle 1994). Consequently, massive stars and ionized gas in these regions may not be cospatial, either.

Another physical effect may also be involved in the comparison of NGC 4214-1 with 30 Dor. The objects differ in their starburst ages (4–5 Myr for NGC 4214-1 versus 3 Myr for 30 Dor), a reasonably secure result. The models predict a dramatic evolutionary difference between the two regions. 30 Dor is a relatively young, unevolved starburst region, which is still at the *beginning* of a phase when powerful W-R winds release copious amounts of energy to the interstellar medium. The models of LH (their Fig. 55) suggest a flat mechanical energy injection rate by stellar winds until $t \approx 3$ Myr. Between 3 and 4 Myr the rate increases by an order of magnitude because of the presence of W-R winds. We propose that 30 Dor has not yet entered the phase of increased energy input, whereas NGC 4214-1 is already beyond it. We speculate that strong stellar winds have swept portions of the interstellar medium out of the NGC 4214-1 starburst. The observed Hα morphology (Fig. 7) is consistent with this suggestion. The region around NGC 4214-1 shows little Hα emission, as expected if most of the gas has been swept out of the central region. The loop structures seen on the Hα image are suggestive of giant shells and filaments formed because of the interaction of winds and interstellar material. As a result, the region is no longer ionization bounded, but rather density bounded. The Hα image of NGC 4214 exhibits an extended, diffuse, patchy structure. We suggest that some of the Lyman continuum photons from NGC 4214-1 may be ionizing the interstellar medium surrounding NGC 4214-1.

We want to emphasize that, while NGC 4214-1 itself may be density bounded, we do not expect this condition to apply to the entire galaxy. Allsopp (1979) mapped neutral hydrogen out to a radial distance of 1.4 Holmberg radii from the center of NGC 4214. The existence of large amounts of neutral hydrogen around NGC 4214 suggests that few if any ionizing photons can escape from the galaxy as a whole—even though individual starburst regions such as NGC 4214-1 may be density bounded. This is in accord with recent direct measurements of the Lyman continuum in four starburst galaxies with the *Hopkins Ultraviolet Telescope* (Leitherer et al. 1995). On average, less than 3% of the produced Lyman continuum photons were found to leak out into the intergalactic medium in the four objects observed.

It is instructive to compare NGC 4214-1 and 30 Dor with the two OB associations OB 48 and OB 78 in M31 (van den Bergh 1964). A stellar census of both associations based on optical spectroscopy and photometry was performed by Massey, Armandroff, & Conti (1986). It was found that the two regions have a rather similar massive star content. The presence of W-R stars in both associations indicates comparable ages as well. Yet Hα images of Pellet et al. (1978) reveal marked differences: OB 48 is situated in a region of strong nebular Hα emission, whereas little emission is detected around OB 78. High-resolution H I observations of M31 by Brinks (1981) reveal a large hole (400 × 800 pc^2) centered on OB 78. The H I hole coincides with the region of low surface brightness Hα emission in the map of Pellet et al. (1978). Most likely, the combined effects of stellar winds and supernovae have created a superbubble, whose interior is nearly devoid of gas. If so, OB 78 would be somewhat more evolved than OB 48 and have a correspondingly higher supernova rate and/or stronger stellar winds. Massey et al. (1986) emphasized the lesson learned from OB 48 and OB 78: despite apparently similar stellar content, local conditions of the interstellar medium in OB 48 and OB 78 are quite different. This may be the result of different conditions in the disk of M31. In addition, differences in the interaction between the ISM and stellar winds and supernovae may contribute. NGC 4214-1 may well be a distant, more luminous counterpart of OB 78 in this respect.

7. DISCUSSION AND CONCLUSIONS

We have presented a detailed analysis of the luminous starburst region NGC 4214-1 using *HST* UV imaging and spectroscopy. NGC 4214-1 is the brightest starburst knot within NGC 4214 in continuum light at optical and UV wavelengths. Although NGC 4214-1 is somewhat more luminous at 1500 Å than the central 30 Dor region, its luminosity is not outstanding when compared with other starburst regions. NGC 4214-1 has an UV luminosity comparable to the starburst knots detected in the central region of He 2–10 (corrected for substantial extinction; Conti & Vacca 1994) and in the sample of starburst galaxies discussed by Meurer et al. (1995). We derive an age of 4–5 Myr and an IMF similar to that in other starburst regions. NGC 4214-1 is further evidence for the suggestion that the observed initial mass function in regions of high-mass star formation is fairly universal (Conti 1994).

NGC 4214 has been studied extensively with various techniques, and several distinct starburst regions have been found. The most relevant studies are those by Hunter (1982), who acquired Hα images and echelle spectroscopy; Huchra et al. (1983), who obtained *IUE* ultraviolet spectra; and SF91, who identified Wolf-Rayet knots from long-slit optical spectra. We find discrepancies between the O-star content of NGC 4214-1 derived from continuum light and from Hα photon counting. Spatial mismatches cannot provide a full explanation for the difference. Rather, the discrepancy is most likely caused by the density-bounded, as opposed to ionization-bounded, nature of NGC 4214-1 . The powerful W-R winds may have swept interstellar gas out of the cluster and established the density bounded conditions.

Is NGC 4214-1 representative for other starburst regions as well? Evidence for large cavities in the interstellar medium around sites of massive star formation has been found from neutral hydrogen measurements, e.g., in the nearby dwarf galaxy Holmberg II (Puche et al. 1992). The cavities in Holmberg II appear to have been created by supernova explosions. They may represent a starburst phase somewhat older than in NGC 4214-1. Calzetti, Kinney, & Storchi-Bergmann (1996) studied the dust obscuration in a sample of 13 starburst galaxies. They concluded from a comparison of optical and near-infrared hydrogen recombination lines that stellar winds *generally* remove the ISM in the immediate surroundings of newly formed massive stars. NGC 4214-1 may be a case where the interstellar gas has been removed as well. NGC 4214-1 serves as a warning, therefore, that Hα photon counting may sometimes give only a lower limit to the number of O stars present.

The reason for the recent starburst in NGC 4214 remains elusive. A plausible suggestion has been made by Hartmann et al. (1986). They found evidence for a highly disturbed velocity field, with an offset between the velocities of the H II regions and the older field population. This could be the result of a recent merger or collision with another system. The dwarf galaxy DDO 113, at a projected distance of about 22 kpc, is nearly within the extended H I envelope. DDO 113 could either be the remnant or an outlying system responsible for the interaction.

We thank Matthew McMaster (STScI) for help with the data reduction of the FOS spectra, and P. Greenfield and R. Jedrzejewski for discussions regarding the reduction of the FOC data. We also thank D. Hunter for providing us with an Hα image of NGC 4214. W. D. V. acknowledges support from a Beatrice Watson Parrent Fellowship at the Institute for Astronomy, University of Hawaii. Support for this work was provided by NASA grant GO-3810 from the Space Telescope Science Institute, which is operated by the Association of Universities for Research in Astronomy, Inc., under NASA contract NAS5-26555.

APPENDIX

DERIVATION OF EQUATIONS (1) AND (2)

The observed count rate (counts s^{-1}) within a circular aperture of radius R centered on a point source is given by

$$F_s = \epsilon(R) F_t + A_s B \,, \tag{5}$$

where $\epsilon(R)F_t$ is the fraction of the total source flux (in counts s^{-1}) contained within the aperture, A_s is the area of the aperture, and B is the background rate per unit area.

The count rate observed in an annular aperture of inner radius R_i and outer radius R_o is similarly given by

$$F_b = [\epsilon(R_o) - \epsilon(R_i)] F_t + A_b B \,, \tag{6}$$

where A_b is the area of the annular aperture.

If we define $\epsilon_s \equiv \epsilon(R)$ and $\epsilon_b \equiv [\epsilon(R_o) - \epsilon(R_i)]$ then we have two equations in terms of the two unknown quantities F_t and B. Equations (1) and (2) follow directly.

The quantities F_s and F_b were directly measured from the FOC images. We used the results presented in Figure 2 to estimate the values of ϵ_s and ϵ_b for the radii of the source and background apertures.

REFERENCES

Allsopp, N. J. 1979, MNRAS, 188, 765
Baxter, D. A. 1993a, in Calibrating *Hubble Space Telescope*, ed. J. C. Blades & S. J. Osmer (Baltimore: STScI), 116
———. 1993b, Instrument Science Report 72, (Baltimore: STScI)
Becker, R., Henkel, C., Bomans, D. J., & Wilson, T. L. 1995, A&A, 295, 302
Binggeli, B., Sandage, A., & Tammann, G. 1987, AJ, 94, 251
Bohlin, R. C. 1993, in Calibrating *Hubble Space Telescope*, ed. J. C. Blades & S. J. Osmer (Baltimore: STScI), 234
Brinks, E. 1981, A&A, 95, L1
Brownsberger, K. R. 1995, Ph.D. thesis, Univ. Colorado
Calzetti, D., Kinney, A. L., & Storchi-Bergmann, T. 1996, ApJ, 458, 132
Chu, Y.-H., & Kennicutt, R. H. 1994, ApJ, 425, 720
Conti, P. S. 1991, ApJ, 377, 115
———. 1994, in Evolution of Massive Stars: A Confrontation between Theory and Observation, ed. D. Vanbeveren, W. van Rensbergen, & C. de Loore (Dordrecht: Kluwer), 37
Conti, P. S., & Massey, P. 1989, ApJ, 337, 251
Conti, P. S., & Vacca, W. D. 1994, ApJ, 423, L97
Crenshaw, D. M., Bruegman, O. W., & Norman, D. J. 1990, PASP, 102, 463

de Vaucouleurs, G., de Vaucouleurs, A., Corwin, H. G., Buta, R. J., Paturel, G., & Fouqué, P. 1991, Third Reference Catalogue of Bright Galaxies (Berlin: Springer)

Dufour, R. J. 1984, in IAU Symp. 108, The Structure of the Magellanic Clouds, ed. S. Van den Bergh & K. S. de Boer (Dordrecht: Reidel), 353

García Vargas, M. L., & Díaz, A. I. 1994, ApJS, 91, 553

Greenfield, P. 1994, Instrument Science Report 75, (Baltimore: STScI)

Hartmann, L. W., Geller, M. J., & Huchra, J. P. 1986, AJ, 92, 1278

Huchra, J. P., Geller, M. J., Gallagher, J., Hunter, D., Hartmann, L., Fabbiano, G., & Aaronson, M. 1983, ApJ, 274, 125

Hunter, D., 1982, ApJ, 260, 81

Jacoby, G. H., et al. 1992, PASP, 599

Jedrzejewski, R. I. 1992, Instrument Science Report 62 (Baltimore: STScI)

Kennicutt, R.C., Jr., & Hodge, P. W. 1986, ApJ, 306, 130

Kinney, A. L., Bohlin, R. C., Calzetti, D., Panagia, N., & Wyse, R. F. G. 1993, ApJS, 86, 5

Kinney, A. L., Calzetti, D., Bica, E., & Storchi-Bergmann, T. 1994, ApJ, 429, 172

Kunth, D., & Joubert, M. 1985, A&A, 142, 411

Leitherer, C., Ferguson, H. C., Heckman, T. M., & Lowenthal, J. D. 1995, ApJ, 454, L19

Leitherer, C., & Heckman, T. M. 1995, ApJS, 96, 9 (LH)

Leitherer, C., Robert, C., & Heckman, T. M. 1995, ApJS, 99, 173 (LRH)

Maeder, A. 1991, A&A, 242, 93

Maeder, A., & Conti, P. S. 1994, ARAA, 32, 237

Maeder, A., & Meynet, G. 1994, A&A, 287, 803

Malumuth, E. M., & Heap, S. R. 1994, AJ, 107, 1054

Marlowe, A. T., Heckman, T. M., Wyse, R. F. G., & Schommer, R. 1995, ApJ, 438, 563

Mas-Hesse, J. M., & Kunth, D. 1991, in IAU Symp. 143, Wolf-Rayet Stars and Interrelationships with Other Massive Stars in Galaxies, ed. K. van der Hucht & B. Hidayat (Kluwer:Dordrecht), 613

Massey, P., Armandroff, T. E., & Conti, P. S. 1986, AJ, 92, 1303

Mathis, J. S., Chu, Y.-H., & Peterson, D. E. 1985, ApJ, 292, 155

Meurer, G. R., Heckman, T. M., Leitherer, C., Robert, C., Kinney, A., & Garnett, D. 1995, AJ, 110, 2665

Moffat, A. F. J., Drissen, L., & Shara, M. M. 1994, ApJ, 436, 183

Muñoz-Tuñon, C. 1994, in Violent Star Formation, ed. G. Tenorio-Tagle (Cambridge: Cambridge Univ. Press), 25

Parker, J. Wm. 1992, Ph.D. thesis, Univ. Colorado

———. 1993, AJ, 106, 560

Pellet, A., Astier, N., Viale, A., Courtès, G., Maucherat, A., Monnet, G., & Simien, F. 1978, A&AS, 31, 439

Puche, D., Westpfahl, D., Brinks, E., & Roy, J.-R. 1992, AJ, 103, 1841

Puls, J., et al. 1996, A&A, 301, 171

Robert, C., Leitherer, C., & Heckman, T. M. 1993, ApJ, 418, 749

Rosa, M., & Mathis, J. S. 1987, ApJ, 317, 163

Rountree, J., & Sonneborn, G. 1993, Spectral Classification with the *International Ultraviolet Explorer*: An Atlas of B-Type Spectra (NASA-RP 1312)

Rowan-Robinson, M. 1985, The Cosmological Distance Ladder (New York: Freeman)

Saha, A., Labhart, L., Schwengler, H., Macchetto, F. D., Panagia, N., Sandage, A., & Tammann, G. A. 1994, ApJ, 425, 14

Sandage, A., & Bedke, J. 1988, Atlas of Galaxies (NASA SP 496)

———. 1994, Carnegie Atlas of Galaxies (Washington: Carnegie Inst. Washington)

Sargent, W. L. W., & Filippenko, A. V. 1991, AJ, 102, 107 (SF91)

Schechter, P. 1980, AJ, 85, 801

Stasińska, G., & Leitherer, C. 1996, ApJS, submitted

Tenorio-Tagle, G., ed. 1994, Violent Star Formation (Cambridge: Cambridge Univ. Press)

Thronson, H. A., Jr., Hunter, D. A., Telesco, C. M., Greenhouse, M., & Harper, D. A. 1988, ApJ, 334, 605

Vacca, W. D. 1992, Ph.D. thesis, Univ. Colorado

———. 1994, ApJ, 421, 140

Vacca, W. D., & Conti, P. S. 1992, ApJ, 401, 543

Vacca, W. D., Robert, C., Leitherer, C., & Conti, P. S. 1995, ApJ, 444, 647

van den Bergh, S. 1964, ApJS, 9, 65

Walborn, N. R., Lennon, D. J., Haser, S. M., Kudritzki, R.-P., & Voels, S. A. 1995, PASP, 107, 104